Am J Cancer Res 2025;15(7):2911-2931
www.ajcr.us /ISSN:2156-6976/ajcr0165988

Original Article

Lactylation-driven molecular taxonomy of melanoma: linking epigenetic modifications to immune evasion and clinical outcomes

Lei Wang[1,2], Xue-Ying Jin[1], Li-Yuan Zhu[2], Yu-Chen Wu[2], Ru-Ning Qiu[2], Li-Feng Feng[2*], Hong-Chuan Jin[2*], Jian-Fang Wang[1*]

[1]Department of Oncology, Shaoxing People's Hospital, The First Affiliated Hospital of Shaoxing University, Shaoxing, Zhejiang, China; [2]Laboratory of Cancer Biology, Key Lab of Biotherapy in Zhejiang Province, Cancer Center of Zhejiang University, Sir Run Run Shaw Hospital, School of Medicine, Zhejiang University, Hangzhou, Zhejiang, China. [*]Equal contributors.

Received May 12, 2025; Accepted July 1, 2025; Epub July 15, 2025; Published July 30, 2025

Abstract: Lactylation, a post-translational modification derived from elevated lactate levels, has gained attention as a potential regulator of melanoma's tumor metabolism and immune responses. Here, we combined single-cell RNA sequencing and bulk transcriptome profiling of cutaneous melanoma samples to establish a lactation-centric prognostic model. Our analyses revealed melanocytes as the most acetylation-enriched cell population and identified a six-gene lactylation signature that stratified patients into high- and low-risk groups with distinct survival outcomes. Mechanistically, high-risk tumors demonstrated significant immunosuppressive features characterized by M2 macrophage accumulation and depleted CD8+ T-cell activity, corresponding to reduced sensitivity to certain chemotherapeutic drugs. Pathway enrichment studies implicated DNA repair, Hedgehog, and JAK-STAT signaling in driving the aggressive phenotype of high-acetylation tumors. Additionally, pseudotime trajectory analyses highlighted developmental shifts in gene expression related to lactylation during melanocyte differentiation. The signature demonstrated robust predictive accuracy in training, testing, and external validation cohorts. Functional validation confirmed the critical role of RAN in promoting proliferation and migration in vitro. These findings unveil lactylation as a critical epigenetic factor influencing melanoma progression and immune evasion, offering a novel prognostic framework and potential therapeutic targets for precision medicine.

Keywords: Lactylation, melanoma, immune microenvironment, multi-omics, prognostic model, single-cell RNA sequencing

Introduction

Cutaneous melanoma is an aggressive malignancy arising from melanocytes, and it remains a leading cause of skin cancer - related mortality due to its high metastatic potential and resistance to conventional therapies [1]. Recent advances in cancer metabolism research have highlighted lactate, a byproduct of aerobic glycolysis (the Warburg effect), as a central factor in shaping the tumor microenvironment (TME) [2]. In melanoma, dysregulated glycolytic flux results in excess lactate production and TME acidification, which drives tumor growth, invasion, and therapeutic resistance through various interconnected mechanisms [3].

Beyond serving as a metabolic byproduct, lactate also exerts profound immunomodulatory effects via protein lactylation - a post-translational modification first identified on histones [4]. Studies have since confirmed lactylation on both histone and non-histone proteins, governed by two distinct mechanisms: enzymatic lactylation, mediated by histone acetyltransferases transferring lactyl groups from lactyl-CoA to lysine residues under hypoxic or inflammatory conditions [5]; and non-enzymatic lactylation, in which tumor-associated lactate spontaneously modifies lysine residues independently of enzyme activity [6-8]. This lactylation process can promote tumor proliferation, invasion, immune evasion, and angiogenesis [9]. Ele-

https://doi.org/10.62347/WJNA8774

vated lactate also suppresses cytotoxic T-cell function and polarizes macrophages toward a tumor-supportive M2 phenotype, underscoring lactylation's dual role as a metabolic intermediate and an immunomodulator [10-14]. Accordingly, multiple preclinical and clinical efforts aim to target lactate dehydrogenase (LDH) or lactate homeostasis to disrupt melanoma progression and potentially enhance immunotherapy outcomes [15, 16].

Single-cell RNA sequencing (scRNA-seq) has revolutionized our ability to dissect tumor heterogeneity and uncover clinically relevant molecular pathways. By combining scRNA-seq with bulk RNA-seq from public repositories, researchers can define cell type-specific mechanisms and identify robust predictive biomarkers [17]. Tools such as SCENIC and CellChat further facilitate the reconstruction of gene regulatory networks and intercellular communication at single-cell resolution [18]. This approach is especially pertinent to melanoma, which exhibits substantial cellular plasticity and distinct immunologic interactions that critically influence patient outcomes.

In this study, we investigated the molecular mechanisms by which lactylation influences melanoma progression and identified a lactylation-related prognostic signature. Integrating scRNA-seq data (GSE215120), bulk transcriptomic data (GSE53118), The Cancer Genome Atlas (TCGA) melanoma cohort (SKCM), and previously validated acetylation-associated genes, we performed comprehensive analyses spanning cell-subtype annotation, ligand-receptor interaction mapping, and regulatory network inference. Subsequently, we constructed and validated a LASSO-Cox-based risk model, examining its associations with immune cell infiltration, drug sensitivity, and critical signaling pathways. Functional characterization reveals RAN as a lactylation-associated driver of proliferation and metastasis. Our findings highlight lactylation as a key epigenetic driver in melanoma, providing a novel risk-stratification framework and potential targets for precision therapeutics.

Materials and methods

Data acquisition

The Gene Expression Omnibus (GEO) database (https://www.ncbi.nlm.nih.gov/geo/), curated by the National Center for Biotechnology Information (NCBI), served as the principal repository for scRNA-seq and bulk transcriptomic datasets. We specifically obtained the scRNA-seq datasets GSE215120, comprising four samples with complete single-cell expression profiles, and GSE115978 which included 20 human melanoma samples. The microarray dataset GSE53118 (annotated on the GPL6884 platform) included survival data from 69 melanoma patients. Additionally, processed transcriptomic data for 473 cutaneous melanoma (SKCM) patients were retrieved from The Cancer Genome Atlas (TCGA) database (https://portal.gdc.cancer.gov/). Lactylation-related genes were extracted from a previously published study [19].

Quality control

Raw scRNA-seq data were processed using the Seurat R package (v4.3.0). We applied three primary filtering criteria: (1) total unique molecular identifiers (UMIs) per cell, (2) number of expressed genes, and (3) mitochondrial gene expression ratio (percentage of mitochondrial gene counts relative to total counts). Cells with elevated mitochondrial gene expression or low RNA content were flagged as potentially apoptotic or stressed. We used the Median Absolute Deviation (MAD) method to remove outliers, excluding data points that deviated by more than 3 MADs from the median for these metrics. This rigorous approach ensured consistent quality for subsequent analyses.

Data standardization and cell annotation

We performed data normalization using the global LogNormalize method, scaling each cell's total expression to 10,000 and then applying a log transformation. Cell-cycle scores were computed with the CellCycleScoring function, and highly variable genes were identified using FindVariableFeatures. The ScaleData function was applied to regress out mitochondrial gene expression percentage, ribosomal gene expression percentage, and cell-cycle phase. Principal component analysis (RunPCA) was then used to identify significant components for further Analysis. To address potential batch effects, we implemented Harmony, followed by nonlinear dimensionality reduction with RunUMAP (Uniform Manifold Approximation and Projection). Cell clusters were anno-

tated by integrating literature-based markers, the CellMarker database, and SingleR, which maps scRNA-seq data to known reference cell types. Genes were filtered with the parameters: only.pos = TRUE, min.pct = 0.25, logfc.threshold = 0.25. This selects only positive marker genes expressed in at least 25% of cells with a minimum log fold-change of 0.25.

Ligand-receptor interaction analysis (CellChat)

We employed CellChat to predict major signaling interactions among distinct cell subtypes [17]. Normalized expression matrices and annotated cell populations were used as inputs. CellChat's network analysis and pattern-recognition algorithms quantified intercellular communication's strength (weight) and frequency (count), revealing functional relationships and disease-specific signaling pathways.

SCENIC analysis

Gene regulatory networks and cell states were reconstructed via the SCENIC pipeline (Single-Cell Regulatory Network Inference and Clustering) [18]. First, co-expression modules were identified using GENIE3 to detect transcription factor (TF) - associated gene sets. Next, motif enrichment analyses were conducted for each module, and TFs were annotated with high or low confidence according to database matches or motif homology. Genes with low motif scores were filtered out, yielding regulons - direct TF-target relationships. Finally, regulon activity was quantified for each cell using the AUCell algorithm, delineating transcriptionally distinct cell states.

Prognostic model construction and survival analysis

We performed univariate Cox regression to identify prognosis-associated genes, then constructed a LASSO (least absolute shrinkage and selection operator) regression model to compute a risk score for each patient. Patients were divided into high- or low-risk groups based on the median risk score. Kaplan-Meier curves and log-rank tests were used to compare survival differences between these groups. LASSO regression and stratified analyses further validated the prognostic value of the risk score, while receiver operating characteristic (ROC) curves evaluated its predictive performance.

Immune cell infiltration analysis

To assess immune cell composition, we applied the CIBERSORT algorithm [20], a deconvolution method based on support vector regression that uses 547 gene expression biomarkers to distinguish 22 immune cell subtypes. Immune infiltration levels were inferred for each sample, and correlations between gene expression profiles and immune cell proportions were subsequently analyzed, elucidating the immune context of each tumor.

Nomogram model construction

We designed a nomogram to integrate the risk score with relevant clinical features, assigning points to each predictor based on its regression coefficient. Summing these points yielded a total score for estimating patient-specific survival probabilities. This graphical approach visualizes the combined prognostic impact of multiple factors and facilitates individualized risk assessment.

Drug sensitivity prediction

Chemotherapy response was predicted using the oncoPredict R package and training data from the Genomics of Drug Sensitivity in Cancer (GDSC) database (https://www.cancerrxgene.org/). Half-maximal inhibitory concentrations (IC50s) were estimated via a regression model with 10-fold cross-validation. We employed the ComBat method [21] to address batch effects and averaged duplicate gene expression values. This approach enabled the correlation of risk scores with chemotherapy sensitivity in melanoma.

Gene set variation analysis (GSVA)

GSVA, a non-parametric and unsupervised method, was used to measure pathway-level enrichment by transforming gene-level expression data into pathway activity scores. We downloaded gene sets from the Molecular Signatures Database (MSigDB v7.0), computed GSVA scores for each sample, and compared pathway activity across groups to investigate relevant biological processes and signaling cascades.

Gene set enrichment analysis (GSEA)

GSEA was conducted to examine pathway differences between high- and low-risk groups.

We used annotated gene sets from MSigDB, ranking differentially expressed genes by their correlation with risk scores. Enriched pathways were identified based on normalized enrichment scores (NES) and adjusted *p-values* < 0.05, providing additional insights into molecular mechanisms associated with each risk group.

Pseudotime trajectory analysis

We employed Monocle [22] to reconstruct cellular differentiation trajectories at the single-cell level. Cells were ordered along a pseudotemporal axis based on transcriptional similarity, revealing transitional states and regulatory gene dynamics throughout the differentiation process. This Analysis highlighted genes marking intermediate or terminal stages of melanocyte development.

Cell culture, RNA extraction, and qRT-PCR

The human melanoma cell lines A375 and SKMEK28 were cultured in DMEM containing 10% fetal bovine serum (FBS), while normal human epithelial keratinocytes (NHEK) were maintained in DMEM/F12 supplemented with 10% FBS and 10 ng/mL epidermal growth factor (EGF). The manufacturer's protocol extracted Total RNA using TRIzol (Invitrogen). RNA concentrations were measured with a Nanodrop 2000C (Thermo Fisher Scientific), and cDNA was synthesized using a ThermoFisher reverse transcription kit. qRT-PCR was performed in a 20 μL reaction volume containing SYBR Green Master Mix (CW0957H, Kangwei) and gene-specific primers. The reaction conditions included 95°C for 10 min followed by 45 cycles at 95°C for 10 s and 60°C for 30 s. Primer sequences for LAP3, RBM39, THRAP3, RAN, DDX3X, S100A11, and the β-actin reference gene are listed in detail below. Relative expression levels were normalized to β-actin.

The gene primer sequences were: Forward 5'-GTCTGGCCGTGAGACGTTT-3', reverse 5'-ACCATAAAAGGTTCGAGTCTTCC-3' for human LAP3; Forward 5'-CAATGCTTGAGGCTCCTTACA-3', reverse 5'-TCCGTTCCTTACTTTTGCTTCTC-3' for human RBM39; Forward 5'-CTCTCTCTCGTTCAAGGAAGCG-3', reverse 5'-CCTCGGAAATCCCGATTCTGAT-3' for human THRAP3; Forward 5'-GGTGGTACTGGAAAAACGACC-3', reverse 5'-CCCAAGGTGGCTACATACTTCT-3' for human RAN; Forward 5'-AGCAGTTTTGGATCTCGTAGTG-3', reverse 5'-ACTGTTTCCACCACGTTCAAAT-3' for human DDX3X; Forward 5'-TGGCAAAAATCTCCAGCCCT-3', reverse 5'-GAAGGGACAGCCTTGAGGAA-3' for human S100A11; Forward 5'-CACCAACTGGGACGACAT-3', reverse 5'-ACAGCCTGGATAGCAACG-3' for human β-actin. Relative expression levels were normalized to β-actin. siRNA sequences were as follows: RAN: siRAN-1: sense: 5'-GUGGCAACAAAGUGGAUAUTT-3', antisense: 5'-AUAUCCACU-UUGUUGCCACTT-3'; siRAN-2: sense: 5'-GUGCCAUCAUAAUGUUUGATT-3', anti-sense: 5'-UCAAACAUUAUGAUGGCACTT-3'.

Cells were incubated in 6-well plates, and transfection was started when cell density reached 60%. Transfection was performed using Lipofectamine RNAiMAX Transfection Reagent (Thermo Fisher Scientific) in all cells maintained in Opti-MEM. The culture medium was replaced with fresh medium supplemented with 10% FBS after 12 h post-transfection. Transfection efficiency was detected using qRT-PCR.

Western blotting

The cells were lysed in RIPA buffer containing protease inhibitors, and the sample was then heated at 100°C in a metal bath for 10 minutes. Subsequently, the same amounts of proteins were separated by 15% sodium dodecyl sulfate-polyacrylamide gel electrophoresis (SDS-PAGE), and then were blotted onto PVDF membrane (Bio-Rad, Hercules, CA, USA). Membranes were incubated with primary antibodies against human RAN (proteintech, 10469-1-AP) and Actin (Santa cruz, sc-7210) at 4°C overnight. Then, membranes were subsequently probed with horseradish peroxidase-conjugated secondary antibodies (Jackson ImmunoResearch; AB_2313567, AB_10015289) for 1.5 h at room temperature. After incubation with chemiluminescent substrate (Thermo Fisher Scientific), protein bands were detected using an Amersham Imager 680 system.

Statistical analysis

All experimental analysis was represented as the mean ± standard deviation (SD) from three times of replicative experiments. Microsoft Excel and GraphPad Prism 5 were used to draw the charts. Survival curves were generated using the Kaplan-Meier method and compared via the log-rank test. A Cox proportional haz-

ards model was applied for multivariate analyses to assess independent prognostic factors. All statistical tests were executed in R (v4.3.0), with *p-values* < 0.05 deemed significant.

Results

Single-cell expression profiling and quality control

We obtained the scRNA-seq datasets GSE-215120, which comprised four cutaneous melanoma (SKCM) tissue samples. The single-cell data from GSE115978 comprises 20 melanoma tissue samples. GSE215120: Quality control was conducted in Seurat (v4.3.0) using three main criteria: (1) cells with fewer than 200 detected genes, (2) mitochondrial gene ratios exceeding three median absolute deviations (MADs), and (3) outlier counts of unique molecular identifiers (UMIs). After filtering 27,314 cells, we removed doublets via DoubletFinder, retaining 13,562 high-quality cells for downstream Analysis (Figure S1A, S1B). Violin and scatter plots illustrated distributions of gene counts, UMIs, and mitochondrial percentages before and after filtering. The top 10 most variable genes were visualized (Figure S1C), demonstrating considerable heterogeneity in the single-cell population. GSE115978: For this dataset, doublets were filtered using the DoubletFinder package following the aforementioned method, resulting in 6,404 cells after filtration. The corresponding violin plots and scatter plots are shown in Figure S3A, S3B. Additionally, the top 10 genes with the highest standard deviation are displayed in Figure S3C.

Identification of 12 cell clusters in melanoma patients

Using principal component analysis (PCA), we identified 20 significant dimensions (ElbowPlot, Figure S1D, S1E). Batch effects were corrected via Harmony (Figure S1F) and UMAP clustering to distinguish 12 unique cell subtypes (**Figure 1A**). Annotation using CellMarker, literature-defined markers, and additional validation assigned these clusters to seven cell populations: Melanocytes, T cells, B cells, Fibroblasts, Endothelial cells, Macrophages, and Keratinocytes (**Figure 1B-D**). Differentially expressed genes (DEGs) (|avg_log2FC| > 0.25, adjusted $P < 0.05$) in each cluster underwent Gene Ontology enrichment, revealing pathways involved in immune regulation and metabolic reprogramming relevant to melanoma biology (**Figure 1E**).

Lactylation interacts with immune cells in melanoma

We initially compiled 330 lactylation-related genes from a published source [19]. Applying AUCell, we measured lactylation activity scores across all single-cell subpopulations and identified melanocytes exhibiting the highest lactylation enrichment and notable intercellular heterogeneity (**Figure 2A**). Further differential gene expression analysis of these melanocytes (|avg_log2FC| > 0.25, $P < 0.05$) yielded 360 marker genes; intersecting these with the 330 lactylation-related genes produced 27 overlapping targets (**Figure 2B**). To evaluate how lactylation modulates intercellular communication, we employed CellChat to infer ligand-receptor interactions across diverse cell subtypes (**Figure 2C**). MIF-(CD74+CXCR4) interactions were highly active between melanocytes and immune or stromal cells (**Figure 2D**), suggesting that acetylation-enriched melanocytes engage in key immunomodulatory signaling within the melanoma TME.

Regulatory network reconstruction via SCENIC

We next performed SCENIC (Single-Cell Regulatory Network Inference and Clustering) on the melanocyte cluster to uncover potential regulatory networks. A heatmap of regulon activity scores across individual cells revealed distinct transcriptional states (**Figure 3A**). Regulons were ranked by their regulon specificity score (RSS), indicating their association with defined cell subgroups. Key regulons identified in lactylation-high melanocytes included YBX1 (+), POLE4 (+), PSMD12 (+), XBP1 (+), and MXD4 (+) (**Figure 3B**, **3C**). Regulons with high RSS values likely orchestrate core transcriptional programs that define melanocyte function and malignant potential.

Prognostic model construction and validation

Using melanoma patient data from TCGA, we performed univariate Cox regression on 27 lactylation-associated genes, identifying seven with prognostic significance ($P < 0.05$) (**Figure 4A**). High LAP3, RBM39, DDX3X, and SUMO2 expression correlated with improved outcomes, whereas elevated RAN, THRAP3, and S100A11 signaled a worse prognosis. Feature selection

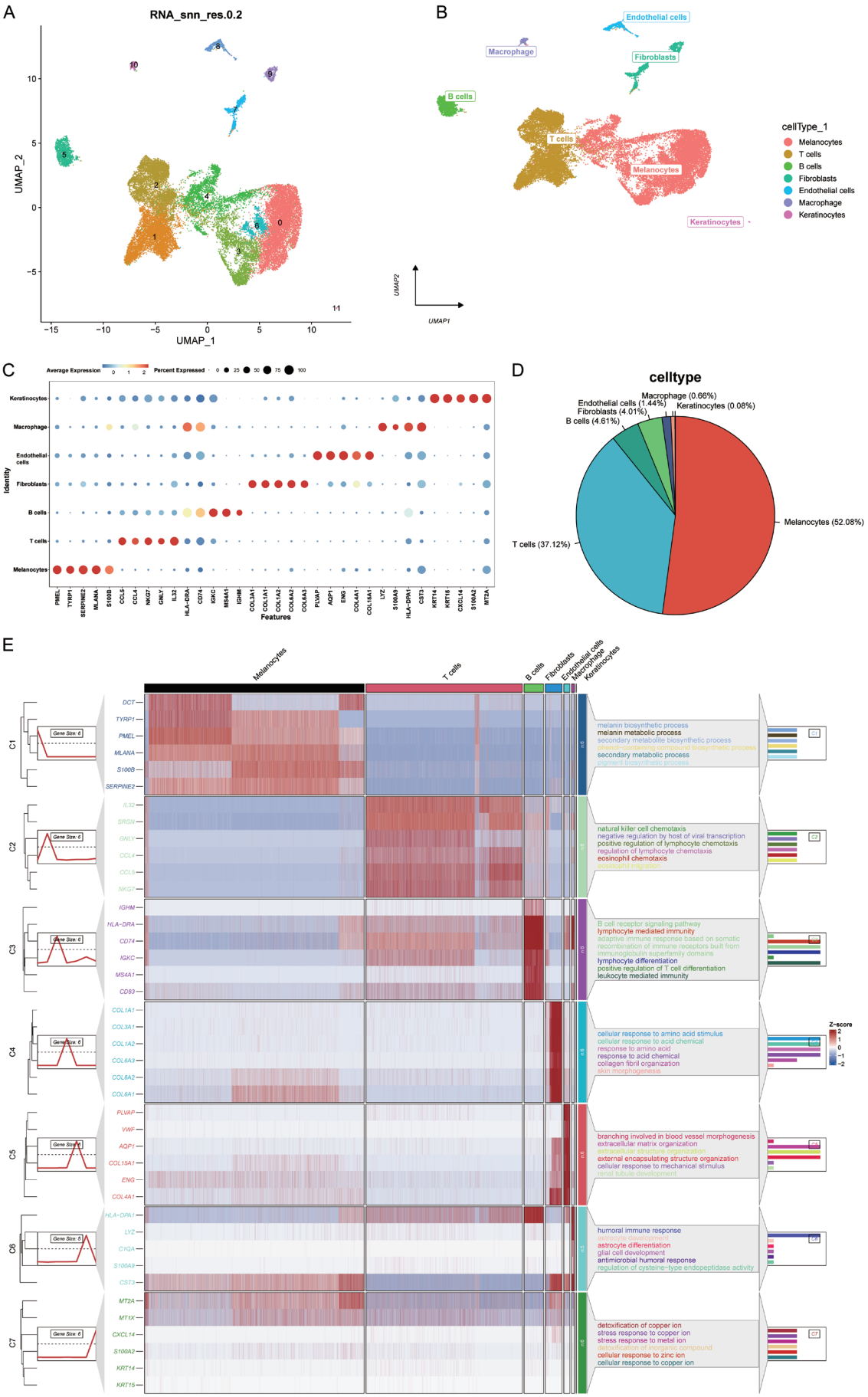
A
RNA_snn_res.0.2
UMAP_1
UMAP_2
B
Endothelial cells
Macrophage
Fibroblasts
B cells
T cells
Melanocytes
Keratocytes
UMAP1
UMAP2
cellType_1
Melanocytes
T cells
B cells
Fibroblasts
Endothelial cells
Macrophage
Keratinocytes
C
Average Expression
Percent Expressed
Keratinocytes
Macrophage
Endothelial cells
Fibroblasts
B cells
T cells
Melanocytes
Identity
Features
PMEL
TYRP1
SERPINE2
MLANA
S100B
CCL5
CCL4
NKG7
GNLY
IL32
HLA-DRA
CD74
IGKC
MS4A1
IGHM
COL3A1
COL1A1
COL1A2
COL6A3
COL6A2
PLVAP
AQP1
ENG
COL4A1
COL18A1
LYZ
S100A9
HLA-DPA1
CST3
KRT14
KRT15
CXCL14
S100A2
MT2A
D
celltype
Macrophage (0.66%)
Endothelial cells (1.44%)
Keratinocytes (0.08%)
Fibroblasts (4.01%)
B cells (4.61%)
Melanocytes (52.08%)
T cells (37.12%)
E
Melanocytes
T cells
B cells
Fibroblasts
Endothelial cells
Macrophage
Keratinocytes
C1
C2
C3
C4
C5
C6
C7
Gene Size: 6
DCT
TYRP1
PMEL
MLANA
S100B
SERPINE2
melanin biosynthetic process
melanin metabolic process
secondary metabolite biosynthetic process
phenol-containing compound biosynthetic process
secondary metabolic process
pigment biosynthetic process
IL32
SRGN
GNLY
CCL4
CCL5
NKG7
natural killer cell chemotaxis
negative regulation by host of viral transcription
positive regulation of lymphocyte chemotaxis
regulation of lymphocyte chemotaxis
eosinophil chemotaxis
eosinophil migration
IGHM
HLA-DRA
CD74
IGKC
MS4A1
CD83
B cell receptor signaling pathway
lymphocyte mediated immunity
adaptive immune response based on somatic recombination of immune receptors built from immunoglobulin superfamily domains
lymphocyte differentiation
positive regulation of T cell differentiation
leukocyte mediated immunity
COL1A1
COL3A1
COL1A2
COL6A3
COL6A2
COL6A1
cellular response to amino acid stimulus
cellular response to acid chemical
response to amino acid
response to acid chemical
collagen fibril organization
skin morphogenesis
Z-score
PLVAP
VWF
AQP1
COL15A1
ENG
COL4A1
branching involved in blood vessel morphogenesis
extracellular matrix organization
extracellular structure organization
external encapsulating structure organization
cellular response to mechanical stimulus
renal tubule development
HLA-DPA1
LYZ
C1QA
S100A9
CST3
humoral immune response
astrocyte development
astrocyte differentiation
glial cell development
antimicrobial humoral response
regulation of cysteine-type endopeptidase activity
MT2A
MT1X
CXCL14
S100A2
KRT14
KRT15
detoxification of copper ion
stress response to copper ion
stress response to metal ion
detoxification of inorganic compound
cellular response to zinc ion
cellular response to copper ion

Figure 1. Cell types and gene expression patterns of melanoma. A. UMAP visualization of single-cell data colored by Leiden cluster assignment (12 clusters). B. Annotations of seven major cell lineages (melanocytes, T cells, B cells, fibroblasts, endothelial cells, macrophages, and keratinocytes) based on marker genes. C. Bubble plot of classic marker genes illustrating their expression across these cell types. Red indicates high expression, and blue indicates low expression. D. Pie chart showing relative proportions of the seven cell types. E. Heatmap displaying log2 fold changes for the top six differentially expressed genes (DEGs) in each subpopulation.

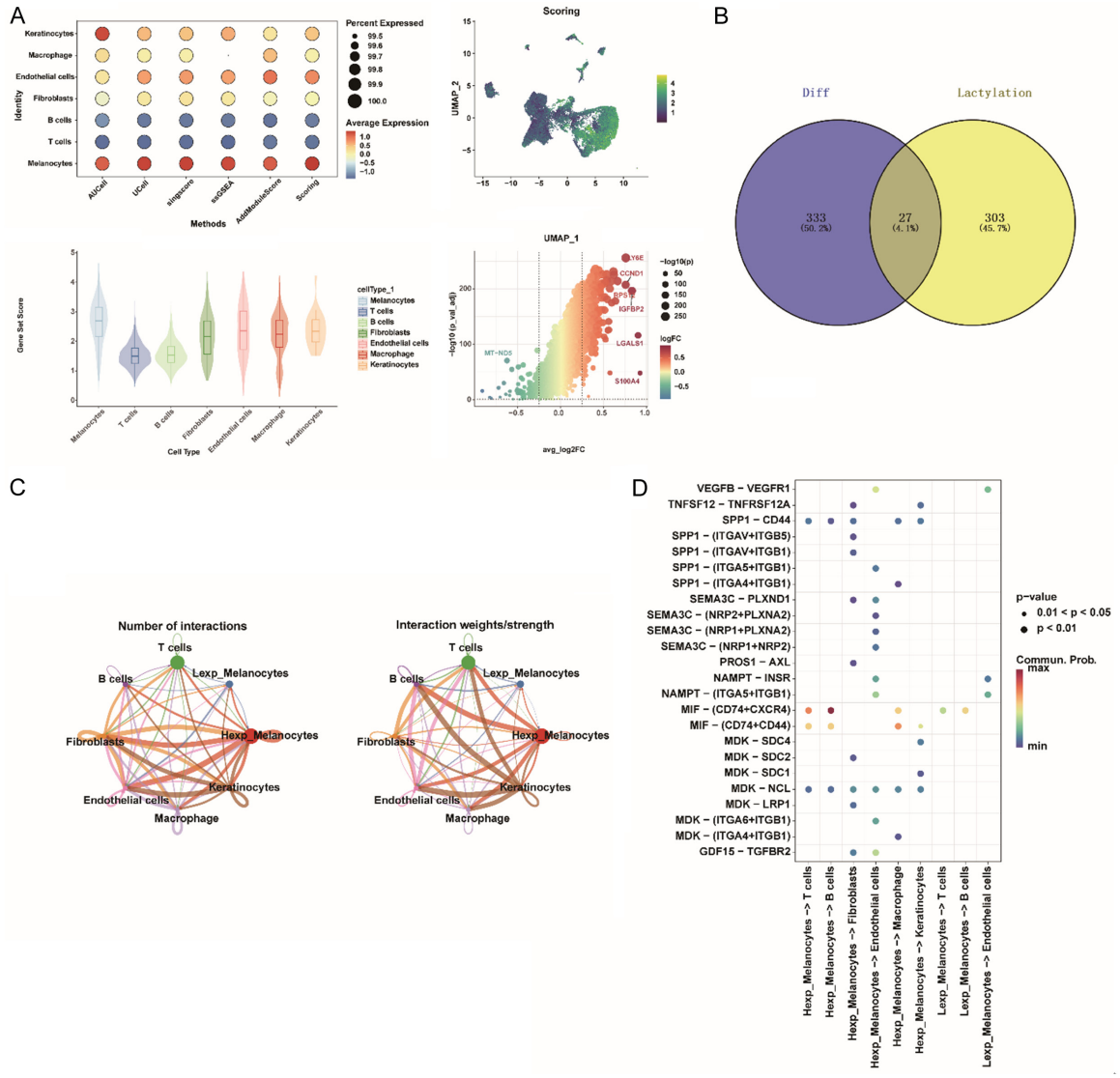

Figure 2. Lactylation-associated cell subtypes and cell-cell communication. A. Bubble plot, Violin plot and Scatter plots showing comparative profiling in melanocyte populations to identify lactylation-enriched cellular subtypes. B. Venn diagram indicating the intersection of differentially expressed lactate-related genes. C. Intercellular communication network among diverse cell populations, visualized by line widths representing interaction strength. D. Bubble plots depicting incoming and outgoing signaling pathways between melanocytes with T cells, B cells and other clusters.

by LASSO regression produced a prognostic signature refined into a risk-scoring formula: Risk Score = (-0.463) × LAP3 + (-0.038) × RBM39 + (0.111) × THRAP3 + (0.149) × RAN + (0.217) × DDX3X + (0.226) × S100A11 (**Figure 4B-D**).

Patients were stratified into high- and low-risk groups according to their risk scores. In both training and testing sets, Kaplan-Meier curves showed significantly poorer overall survival (OS) for high-risk patients (**Figure 4E**, **4F**). ROC

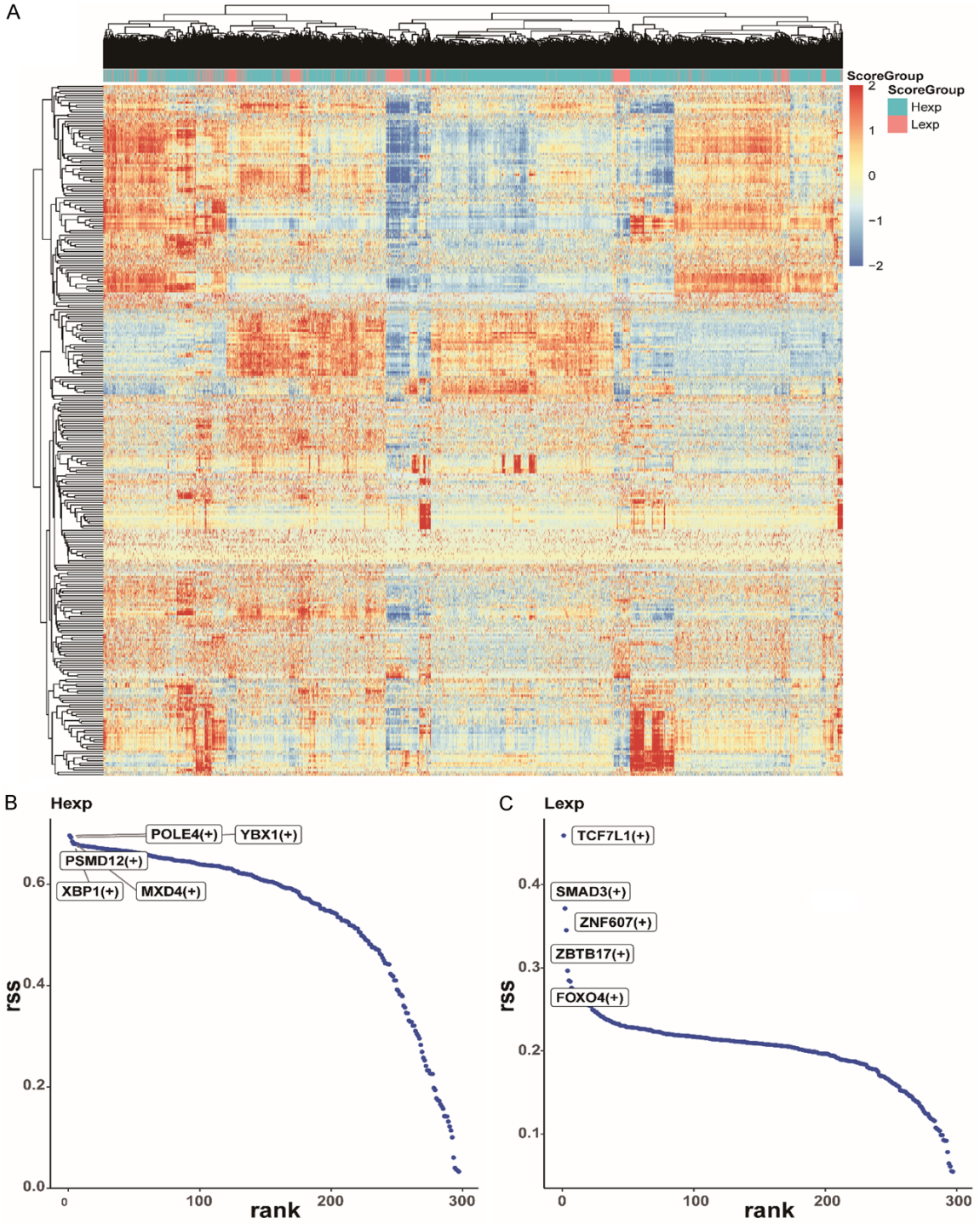

Figure 3. SCENIC analysis in melanocytes. A. Heatmap of regulon activity scores in individual melanocyte cells, indicating distinct transcriptional states. B. Scatter plot ranking transcription factors by regulon specificity score (RSS) in high-expression melanocytes (Hexp). C. Scatter plot ranking transcription factors by RSS in low-expression melanocytes (Lexp).

curves demonstrated strong predictive accuracy (**Figure 4G**, **4H**). The external dataset GSE53118 confirmed these findings, underscoring the model's generalizability (**Figure 4I**).

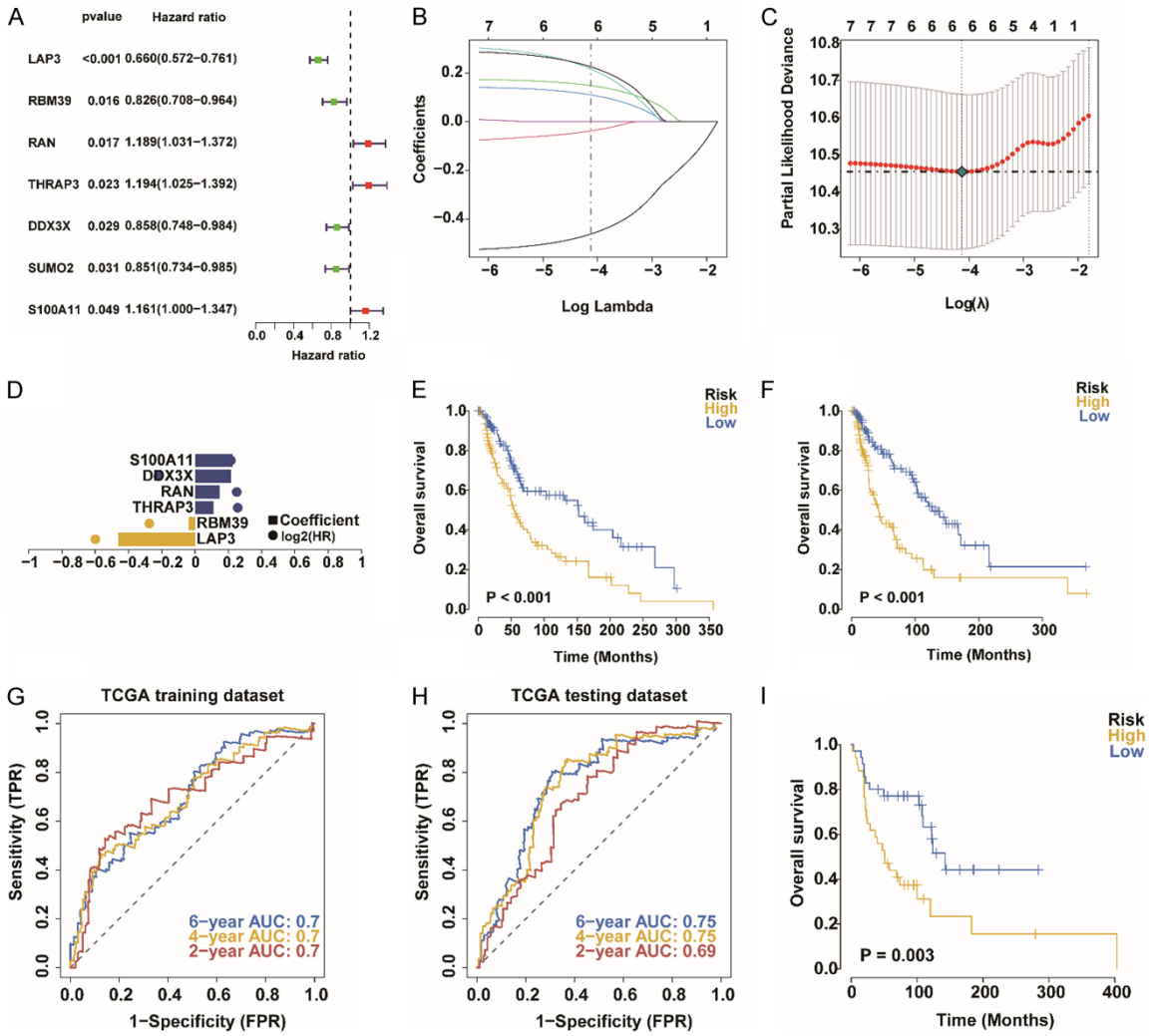

Figure 4. Prognostic model construction and validation. A. Forest Plot of seven prognostic genes (*P < 0.05*) from an initial list of 27 lactylation-related genes using univariate Cox regression. B-D. LASSO regression screening to refine these genes into a six-gene signature. E, F. Kaplan-Meier survival curves showing significantly lower overall survival (OS) in the high-risk group compared with the low-risk group for both training and testing cohorts. Statistical significance was determined by the Log-rank test *(P < 0.001)*. G, H. ROC curves demonstrating strong predictive accuracy at 2, 4, and 6 years in the training and testing sets. The AUC values range between 0.5 and 1, where 0.5 indicates no discriminative ability and 1 represents perfect discriminative ability. I. External validation in the GSE53118 GEO dataset, confirming poorer OS for the high-risk group.

Relationship between risk score and the immune microenvironment

Given that the tumor microenvironment (TME) profoundly influences melanoma progression, we evaluated correlations between risk scores and immune cell infiltration. CIBERSORT-based deconvolution showed distinct immune subsets in high- versus low-risk groups (**Figure 5A**, **5B**). In particular, eosinophils, macrophages (M0, M1, and M2), monocytes, and resting and activated NK cells varied significantly between groups (**Figure 5C**). The risk score was positively correlated with immunosuppressive cell types (M0 and M2 macrophages) and inversely associated with cytotoxic CD8+ T cells and activated CD4+ memory T cells (**Figure 5D**). These data suggest that high-risk melanomas harbor a more immunosuppressive TME, potentially driving enhanced tumor progression and resistance to therapy.

Nomogram model for prognostic prediction

Patients were categorized into high- and low-risk cohorts based on the median risk score.

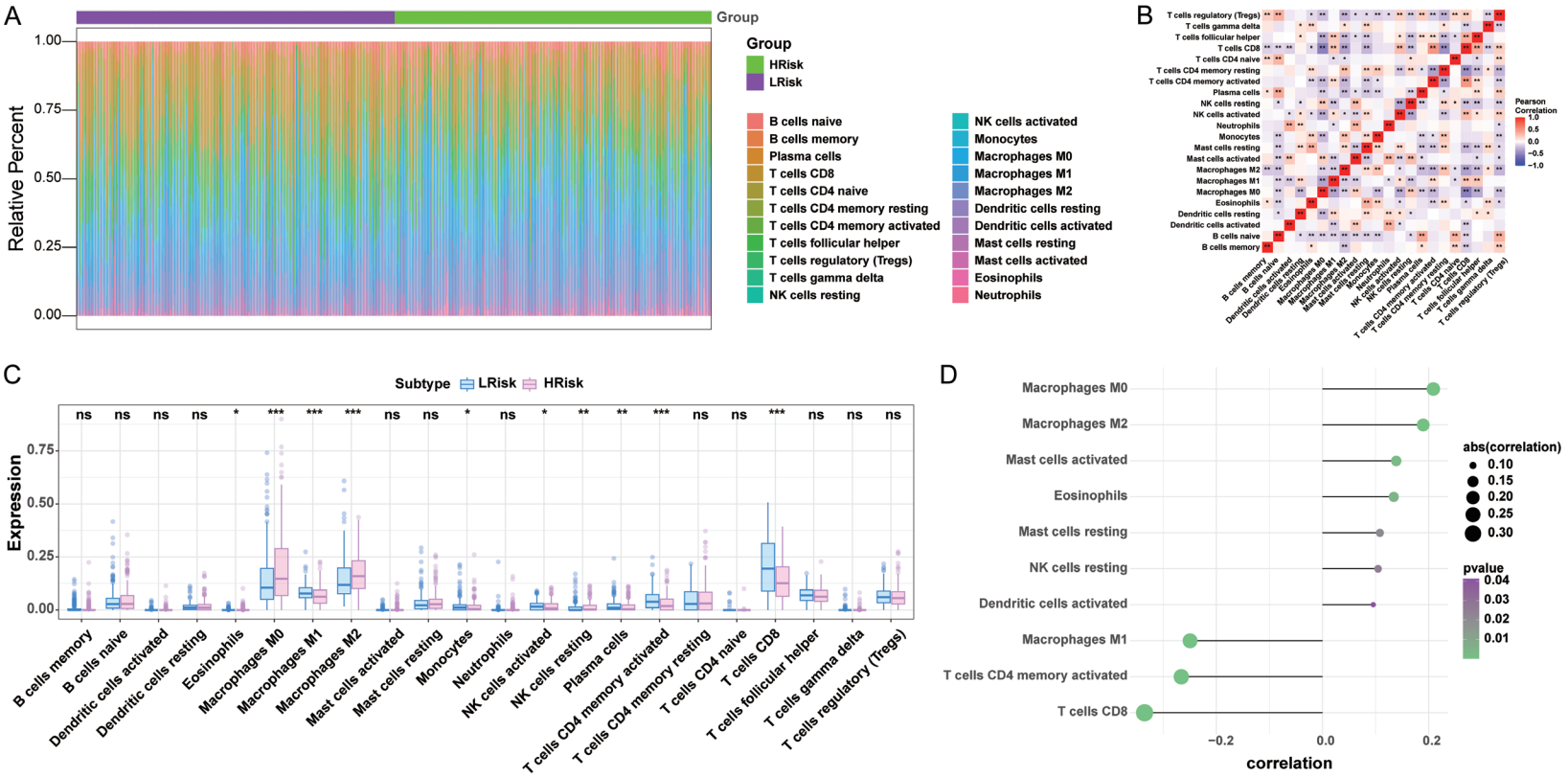

Figure 5. Correlation of the risk model with immune microenvironment. A. CIBERSORT-based immune cell composition in high- and low-risk patient groups. B. Heatmap illustrating correlations among immune cell subsets. C. Boxplots highlighting statistically significant differences in immune cell proportions between high- and low-risk tumors. D. Lollipop plot showing a positive correlation of the risk score with immunosuppressive macrophages (M0, M2) and a negative correlation with cytotoxic T cells.

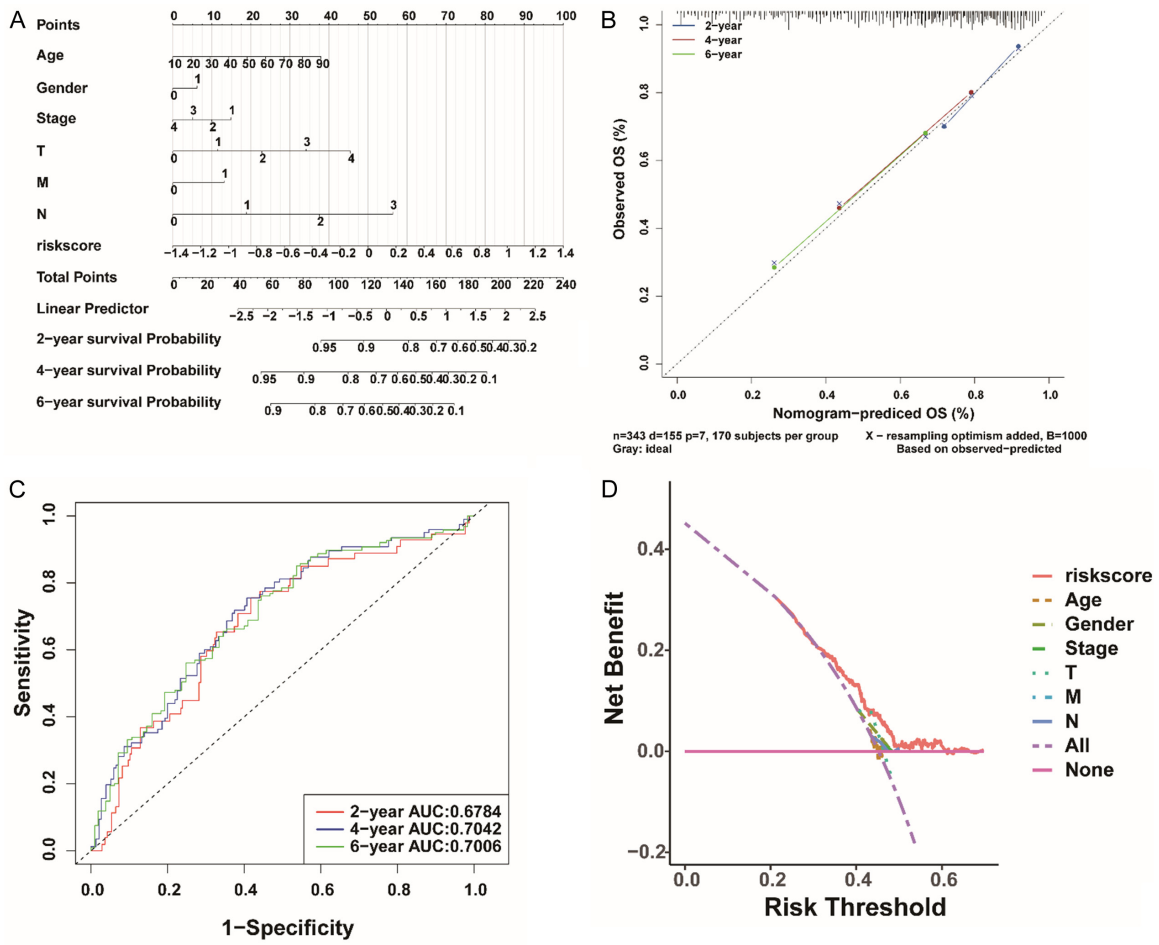

Figure 6. Nomogram model for individualized prognostic prediction. A. Nomogram integrating the lactylation-driven risk score with clinicopathological variables to estimate survival probabilities. B. Calibration curve comparing predicted and observed survival outcomes in melanoma patients. C. Time-dependent ROC curves (2-, 4-, and 6-year) indicating the nomogram's discriminative accuracy (AUCs: 0.6784, 0.7042, 0.7006). Shaded regions denote 95% confidence intervals. D. Decision curve analysis (DCA) demonstrating a superior net benefit of the nomogram versus conventional staging.

We built a nomogram integrating risk score with clinical parameters to visually estimate individual survival probabilities (**Figure 6A**, **6B**). Logistic regression demonstrated that the risk score significantly improved the nomogram's predictive performance *(P < 0.001)*. Predictions at 2-, 4-, and 6-year endpoints showed robust discriminative ability (AUCs: 0.6784, 0.7042, 0.7006; **Figure 6C**), and decision curve analysis (DCA) indicated superior net benefit over standard staging systems (**Figure 6D**).

Drug sensitivity correlation analysis

Early-stage cutaneous melanoma often benefits from surgery combined with chemotherapy. Using the oncoPredict R package, we assessed half-maximal inhibitory concentrations (IC50) for common chemotherapy agents, based on drug sensitivity data from the Genomics of Drug Sensitivity in Cancer (GDSC) repository. We discovered significant associations between the risk score and responses to vinblastine_1004, paclitaxel_1080, and vincristine_1818 (**Figure 7A**). Specifically, high-risk patients exhibited increased IC50 values for these drugs (*P < 0.01*), indicating diminished therapeutic effectiveness under high-acetylation conditions and reinforcing the need to tailor treatment strategies according to lactylation status.

Functional pathway analyses of high- and low-risk groups

To dissect the molecular mechanisms underlying tumor progression in each risk category, we conducted GSVA and GSEA. In the high-risk

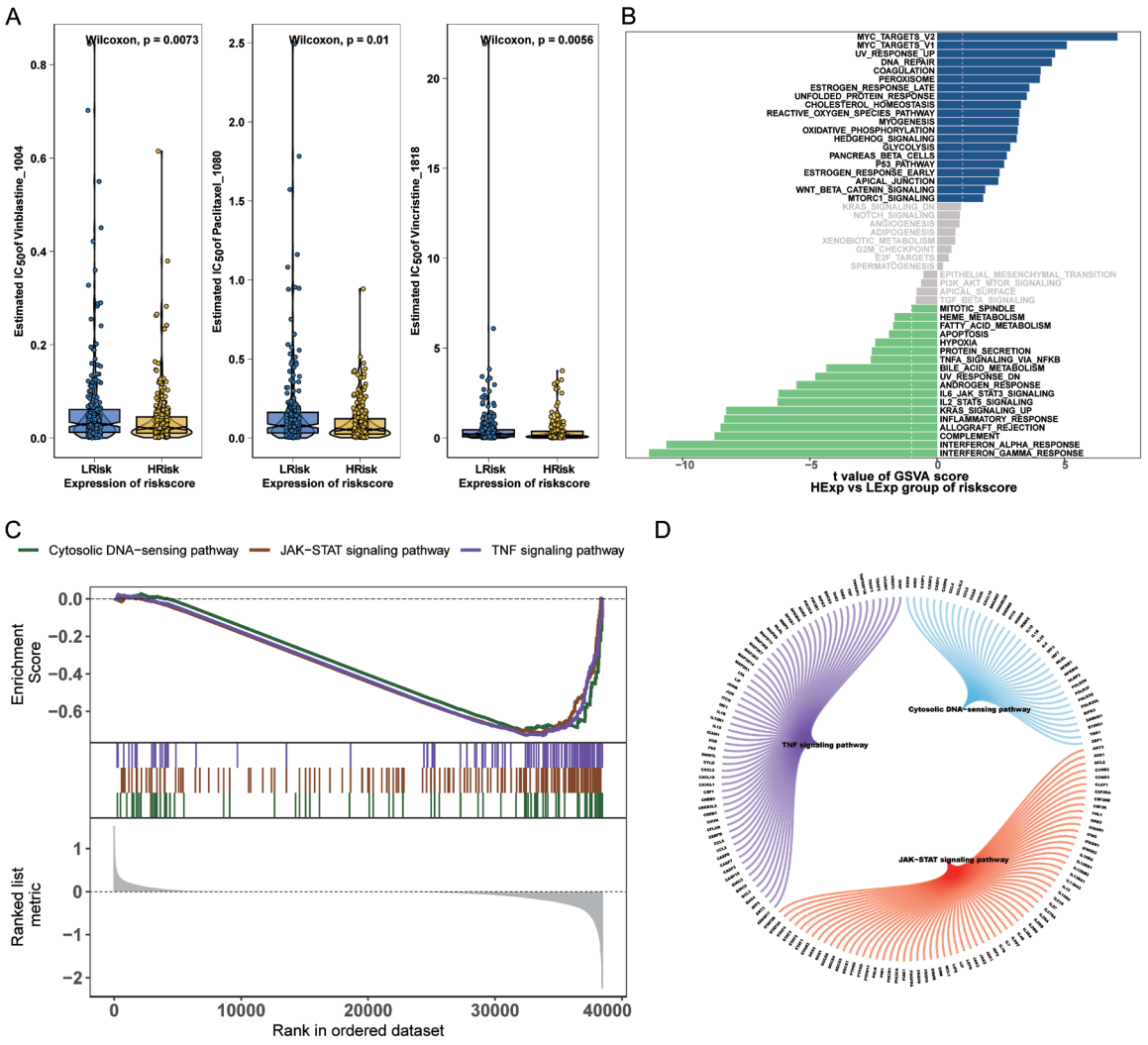

Figure 7. Drug sensitivity and associated signaling pathways. A. Predicted chemotherapy response (IC50) using the oncoPredict R package, anchored by GDSC database profiles. High-risk patients showed reduced sensitivity (elevated IC50) to vinblastine_1004, paclitaxel_1080, and vincristine_1818 ($P \leq 0.01$). B, C. GSVA and GSEA highlighting distinct enrichment of pathways (DNA repair, Hedgehog, JAK-STAT) in high- versus low-risk groups. D. A molecular interaction network illustrating cross-talk among these enriched pathways.

group, GSVA revealed enrichment in DNA repair, Hedgehog signaling, and p53-related pathways (**Figure 7B**). GSEA further highlighted differential activation of the cytosolic DNA-sensing pathway, TNF signaling, and JAK-STAT signaling (**Figure 7C**). We constructed a molecular interaction network depicting cross-talk among these pathways (**Figure 7D**), emphasizing their potential synergistic roles in driving high-risk tumor phenotypes.

Expression and pseudotime analysis of model genes

We visualized the expression distribution of six model genes (LAP3, RBM39, THRAP3, RAN, DDX3X, S100A11) in single-cell clusters (**Figure 8A**, **8B**). Pseudotime trajectory analysis on melanocytes placed cells along a developmental axis, with states color-coded by pseudotime, branch-specific clustering, and risk stratification (**Figure 9A-C**). Early differentiation markers (BCAN, LIMD1, HMCN1) were prominent at the initial stages, whereas late-stage markers (MITF, KCNJ13, AFF3) predominated at terminal points (**Figure 9D**). Model gene expression showed varied trajectories: DDX3X progressively increased, while LAP3, RAN, and S100A11 peaked at mid-differentiation, and RBM39 and THRAP3 demonstrated U-shaped patterns (**Figure 9E**).

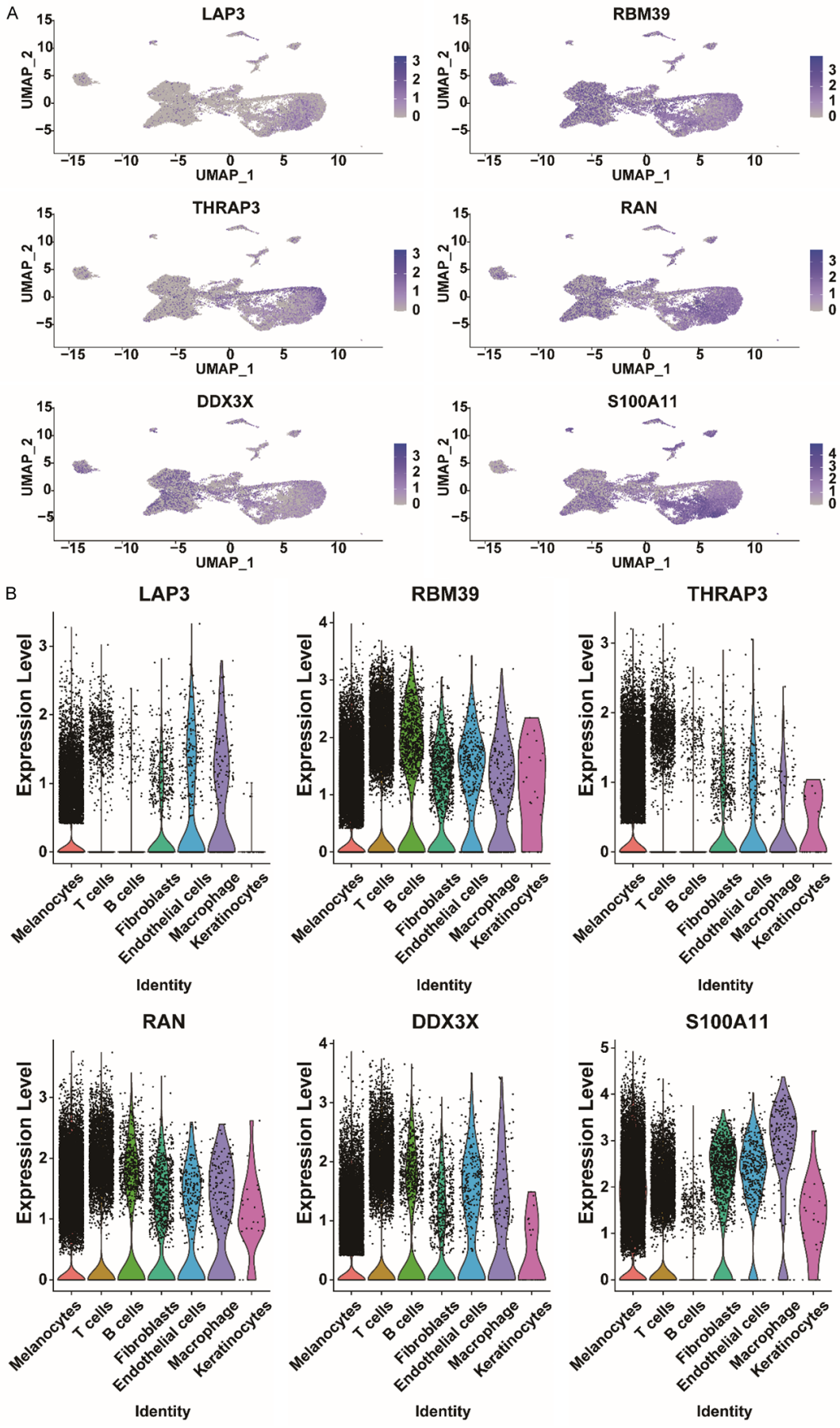
A
LAP3
RBM39
THRAP3
RAN
DDX3X
S100A11
UMAP_1
UMAP_2
B
Expression Level
Identity
Melanocytes
T cells
B cells
Fibroblasts
Endothelial cells
Macrophage
Keratinocytes

Figure 8. Model gene expression in single cells. A, B. DotPlot and Violin Plot visualizing expression patterns of the six model genes (LAP3, RBM39, THRAP3, RAN, DDX3X, S100A11) across melanoma single-cell clusters.

Validation of key gene expression profiles and multi-algorithm quantification of lactylation scores in single-cell data

To further validate our results, we first processed the single-cell data (GSE115978). The optimal number of principal components (PCs) was determined as 20 using an ElbowPlot (Figure S3D). PCA dimensionality reduction revealed the presence of batch effects between samples (Figure S3E). Following dimensionality reduction via Uniform Manifold Approximation and Projection (UMAP), 17 distinct clusters were identified (Figure S3F). These 17 clusters were annotated into 8 major cell types - Fibroblast cells, Myeloid cells, T cells, Melanocytes, B cells, Keratinocytes, Endothelial cells, and Cycling cells (proliferating cells) - based on established cell markers (Figure S4A). Dot plots illustrating the expression of canonical markers for these 8 cell types (Figure S4B) and stacked bar charts showing their proportional distribution across groups (Figure S4C) are provided.

Subsequently, we analyzed the expression profiles of key genes within the single-cell dataset. The expression patterns of these key genes across the annotated cell types (Fibroblast cells, Myeloid cells, T cells, Melanocytes, B cells, Keratinocytes, Endothelial cells, and Cycling cells) are depicted in Figure S5A, S5B.

We then employed the AUCell, UCell, singscore, ssGSEA, and AddModuleScore algorithms to quantify lactylation scores at the scRNA-seq level (Figure S5C). By averaging the scores derived from these methods to assess expression across different cell types, we observed that melanocytes consistently exhibited significantly elevated lactylation levels (Figure S5D).

Validation of prognostic gene expression in vitro

To confirm the expression patterns of LAP3, RBM39, THRAP3, RAN, DDX3X, and S100A11 in melanoma cells, we performed qRT-PCR using gene-specific primers. S100A11 was highly expressed in A375 and SK-MEL28 cells, whereas LAP3, RBM39, RAN, THRAP3, and DDX3X were abundant in HNEK cells (**Figure 10A-F**). These results corroborate the transcriptomic data, lending further support to the prognostic relevance of the signature genes.

RAN plays a critical role in melanoma proliferation and migration

Based on GEPIA (http://gepia.cancer-pku.cn), box plots showed that RAN expression was significantly up-regulated in 461 skin cutaneous melanoma tissues compared with 558 normal tissues (**Figure 10G**), and the Kaplan-Meier survival curves showed that the prognosis of the RAN high-expression group was significantly worse than that of the RAN low-expression group (**Figure 10H**). Therefore, RAN was knocked down in A375 and SKMEL28 cells, and the knockdown efficiency was validated by qPCR and Western blotting (**Figure 10I**, **10J**). In the time-lapse proliferation assay, RAN knockdown (siRAN1/2) significantly suppressed cell proliferation at 12, 24, 48 and 72 hours compared to the siNC group (**Figure 10K**). Furthermore, in the scratch wound healing assay, siRAN1/2 knockdown markedly inhibited melanoma cell migration (**Figure 10L**).

Metabolic-immune crosstalk of model genes

To elucidate potential links between these model genes, metabolic pathways, and immune modulation, we employed AUCell-based analyses (Figure S2). THRAP3 and S100A11 showed high activity in oxidative phosphorylation and MYC target pathways, aligning with roles in metabolic reprogramming. RBM39 was significantly enriched in allograft rejection and NF-κB-mediated TNFA signaling, indicating a function in immune escape and inflammation. Meanwhile, RAN and LAP3 also exhibited increased oxidative phosphorylation and MYC target activation, and DDX3X was highly associated with TGF-β and NF-κB-driven TNFA signaling. These data suggest that the signature genes operate at the intersection of metabolic adaptations and immunosuppressive mechanisms, reinforcing their significance in melanoma progression.

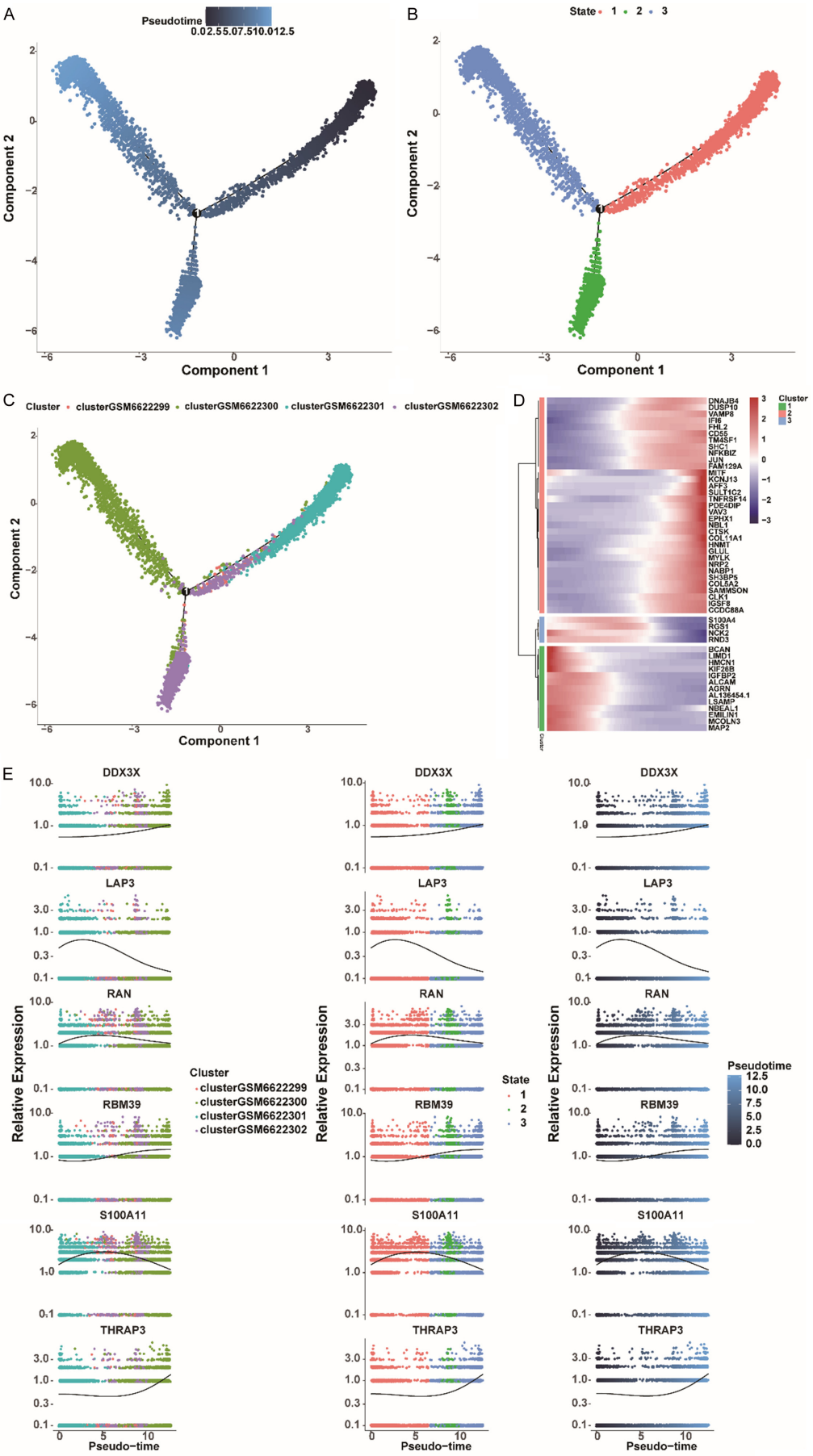
A
Pseudotime
0.02.55.07.510.012.5
Component 2
Component 1
B
State 1 2 3
Component 2
Component 1
C
Cluster clusterGSM6622299 clusterGSM6622300 clusterGSM6622301 clusterGSM6622302
Component 2
Component 1
D
Cluster
1
2
3
DNAJB4
DUSP10
VAMP8
IFI6
PHL2
CD55
TM4SF1
SHC1
NFKBIZ
JUN
FAM129A
MITF
KCNJ13
AFF3
SULT1C2
TNFRSF14
PDE4DIP
VAV3
EPHX1
NBL1
CTSK
COL11A1
HNMT
GLUL
MYLK
NRP2
NABP1
SH3BP5
COL5A2
SAMMSON
CLK1
IGSF8
CCDC88A
S100A4
RGS1
NCK2
RND3
BCAN
LIMD1
HMCN1
KIF26B
IGFBP2
ALCAM
AGRN
AL136454.1
LSAMP
NBEAL1
EMILIN1
MCOLN3
MAP2
E
DDX3X
LAP3
RAN
RBM39
S100A11
THRAP3
Relative Expression
Pseudo−time
Cluster
clusterGSM6622299
clusterGSM6622300
clusterGSM6622301
clusterGSM6622302
State
1
2
3
Pseudotime
12.5
10.0
7.5
5.0
2.5
0.0

Figure 9. Pseudotime trajectory analysis of model genes. A. Pseudotime ordering of melanocytes, illustrating transitional states during differentiation. B. Distribution of cells across distinct states. C. Cluster assignments along the pseudotime axis, indicating transcriptional shifts among subpopulations. D. Heatmap of gene expression patterns at various stages, capturing early (BCAN, LIMD1, HMCN1) and late markers (MITF, KCNJ13, AFF3). E. Expression trends of model genes, highlighting mid-stage peaks (LAP3, RAN, S100A11) and U-shaped behaviors (RBM39, THRAP3).

Discussion

Cutaneous melanoma remains among the most lethal skin cancers worldwide, with its rising incidence and mortality attributed to high metastatic potential and resistance to standard therapies. Although targeted treatments (e.g., BRAF/MEK inhibitors) and immunotherapies (e.g., PD-1/PD-L1 inhibitors) have improved patient outcomes, significant heterogeneity persists. Existing prognostic systems (e.g., AJCC staging) do not capture the molecular and epigenetic complexities that critically influence disease progression and treatment response. To address this limitation, our study constructed a lactylation-related prognostic model that integrates risk scores with clinical variables, enabling refined stratification of patients and revealing immunosuppressive tumor microenvironment (TME) features in high-risk melanomas. By linking lactylation to melanoma prognosis, this work advances the understanding of how metabolic and epigenetic dysregulation contributes to clinical outcomes.

In recent years, prognostic model development in oncology has benefited greatly from multi-omics integration, machine learning, and robust clinical data curation. For instance, combining tumor mutation profiles with immune-related gene signatures can enhance the prediction of immunotherapy responsiveness [23]. Increasing evidence places lactate and histone lactylation at the intersection of metabolic plasticity and immune suppression in cancer [24, 25]. This modification can modulate chromatin accessibility, influencing oncogenic pathways and immune evasion strategies. In melanocytes, the role of histone lactylation in stabilizing MITF expression further underscores the potential of lactylation to drive tumor initiation and progression [26-28]. Consequently, lactylation-associated genes have emerged as essential biomarkers for diverse malignancies, including melanoma [29-33]. Consistent with this paradigm, our study identified six acetylation-linked genes (LAP3, RBM39, THRAP3, RAN, DDX3X, S100A11) that predict survival and correlate with chemotherapy sensitivity. These genes collectively drive key oncogenic processes including proliferation, metastasis, immune evasion, metabolic reprogramming, therapy resistance, and genomic instability in aggressive cancers [34-42]. Mechanistically, high-risk melanomas exhibit activation of pathways central to immune suppression and metastasis. Functional validation confirmed RAN as a critical driver of melanoma proliferation and migration. RAN, a GTPase involved in nucleocytoplasmic transport and mitotic spindle assembly, is frequently overexpressed in cancers and linked to metastatic dissemination [43]. Single-cell and transcriptomic validation confirmed the expression dynamics of these genes in melanoma, providing a foundation for mechanistic exploration. Additionally, SCENIC analysis was employed to uncover core biological regulatory mechanisms, pinpointing key transcription factors (TFs) and their target genes. We identified YBX1 and POLE4 as master regulons in lactylation-enriched melanocytes. For instance, LINC01419 binds YBX1 to stabilize PDK1 mRNA, amplifying lactate production via enhanced transcript stability - a process potentially amplified by lactylation-mediated TF recruitment [44]. Heatmap visualization of regulon activity revealed heterogeneous transcriptional states across melanocyte subpopulations, underscoring the interplay between lactylation and cellular plasticity. In parallel, we validated our key genes and the elevated lactylation levels in melanoma using an independent single-cell dataset. Therefore, these findings provide novel insights into melanoma pathogenesis, immune microenvironment dynamics, and precision therapeutics.

Lactylation-related gene prognostic models have emerged as powerful tools in cancer research and clinical practice, offering novel insights into tumor biology, patient stratification, and therapeutic decision-making. TME is a key determinant of melanoma progression and therapeutic response. Immune infiltration in cutaneous melanoma represents a complex interplay of anti-tumor defense and pro-tumor

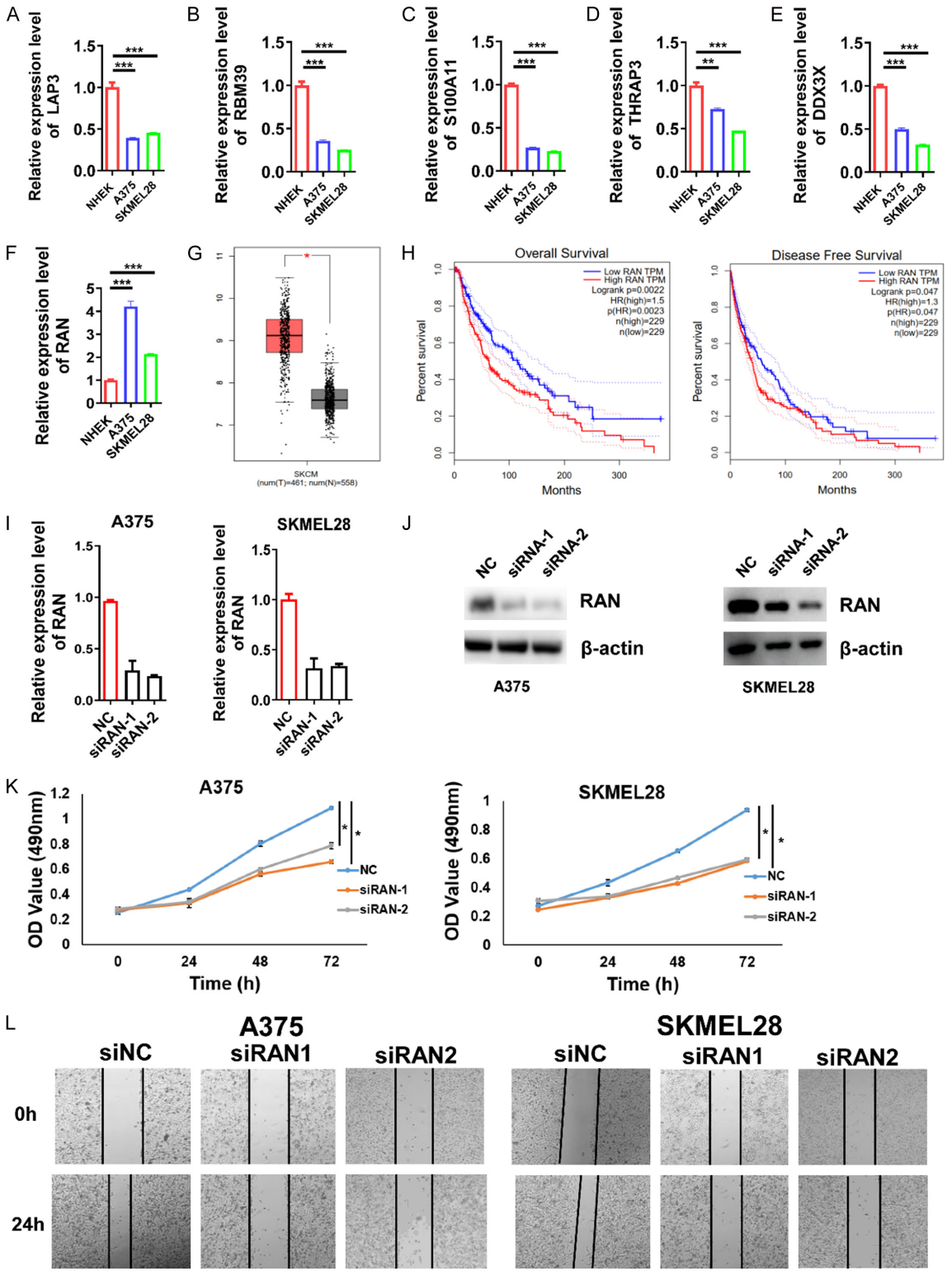

Figure 10. RAN as a critical driver of melanoma proliferation and migration. A-F. qRT-PCR validation of the expression of four genes (LAP3, RBM39, S100A11, RBM39, THRAP3, DDX3X and RAN) in A375, SK-MEL-28, and NHEK cells. G. Box plots showing RAN expression in 461 skin cutaneous melanoma tissues vs 558 normal tissues based on GEPIA (http://gepia.cancer-pku.cn). H. Survival Curve plots demonstrating the impact of RAN on overall survival (OS) and disease-free survival (DFS) in melanoma based on GEPIA (http://gepia.cancer-pku.cn). I. The knockdown efficiency of RAN in A375 and SKMEL28 cells transfected with siRNA1/2 was detected using qRT-PCR. J. The knockdown efficiency of RAN in A375 and SKMEL28 cells transfected with siRNA1/2 was detected using Western Blotting. K. Proliferative capacity was detected by MTS assay. L. Wound healing assay was used to detect the migration ability. Data are shown as mean ± SD from three independent experiments. Significance is indicated by *$P < 0.05$.

adaptation, shaping both disease progression and therapeutic outcomes. Recent studies highlight the dual role of immune cells: while cytotoxic CD8+ T cells and M1 macrophages exert antitumor effects, regulatory T cells (Tregs) and M2 macrophages promote immune evasion [45, 46]. Clinically, immune infiltration patterns serve as biomarkers, with high CD8+/Treg ratios predicting immune checkpoint inhibitors (ICIs) efficacy [47], while elevated MDSCs correlate with BRAF/MEK inhibitor resistance [48]. Emerging strategies target metabolic competition (e.g., lactate-driven CD8+ T-cell dysfunction) [49] and spatial immune exclusion (e.g., Wnt/β-catenin-mediated chemokine suppression) [50], employing CSF1R inhibitors [51], CD40 agonists [52], and LAG-3/TIM-3 blockers [53] to reprogram the TME. Technological advances, including single-cell RNA-seq and spatial transcriptomics, reveal dynamic immune evolution during therapy and identify perivascular T-cell niches as predictors of ICIs response. Despite progress, challenges persist in longitudinal monitoring of TME plasticity and integrating immune signatures with mutational burden for precision immunotherapy. Future directions focus on disrupting lactate-mediated immunosuppression and leveraging epigenetic modifiers to rebalance immune infiltration, offering hope for personalized therapeutic breakthroughs. Our findings align with these observations, revealing that high-risk melanomas exhibit elevated M2 macrophage infiltration and CD8+ T-cell depletion. Notably, we identified lactylation as a novel modulator of this immunosuppressive shift. Lactate accumulation, driven by glycolytic reprogramming in melanocytes, may polarize macrophages toward an M2 phenotype via histone lactylation, as suggested by the enrichment of MIF-(CD74+CXCR4) interactions [54, 55]. MIF secretion by melanocytes binds to CD74 on macrophages, triggering CXCR4-dependent PI3K/AKT signaling, which stabilizes HIF-1α and further amplifies glycolytic flux in TAMs-a vicious cycle sustaining lactate production [56]. This suggests lactylation may reinforce immune evasion by sustaining MIF signaling, a hypothesis that warrants experimental validation. This aligns with prior reports that lactate-induced histone lactylation reprograms myeloid cells toward immunosuppressive states [57]. The differential drug sensitivity profiles between risk groups suggest that lactylation-high melanomas may benefit from combinatorial strategies targeting lactate metabolism. For instance, LDH inhibitors or monocarboxylate transporter (MCT) blockers could synergize with chemotherapy by normalizing the TME [58]. Furthermore, the association between RBM39 and NF-κB activation points to proteasome inhibitors as potential adjuvants to disrupt lactylation-driven survival signaling. High-risk melanomas exhibited enrichment of oxidative phosphorylation (OXPHOS) and MYC targets-a paradoxical finding in light of the Warburg effect. This may reflect mitochondrial retrograde signaling, where lactate-derived acetyl-CoA fuels histone acetylation, priming chromatin for lactylation-dependent transcription [59]. MYC activation further enhances glutamine uptake, supporting nucleotide synthesis for rapid proliferation [60]. By integrating risk scores with clinical variables, our nomogram offers a practical tool for personalized prognosis and therapy selection.

While this study advances our understanding of lactylation in melanoma, several limitations deserve attention. First, the lactylation-associated genes were derived from colorectal cancer studies, necessitating experimental validation (e.g., ChIP-seq, lactylation-specific antibodies) to confirm their relevance in melanoma. Second, the scRNA-seq cohort (n = 4) lacks racial and etiological diversity, potentially biasing subtype annotations. Third, the prognostic model requires prospective validation in clinical trials to assess its utility in guiding immunotherapy decisions. Future work could explore spatial transcriptomics to map lactylation gradients within the TME and investigate the role of lactylation in resistance to immune checkpoint inhibitors.

In summary, this study delineates a lactylation-centric framework for understanding melanoma progression, uniting metabolic dysregulation, epigenetic reprogramming, and immune suppression. The prognostic signature and mechanistic insights offer a foundation for developing lactate-targeted therapies and refining risk-adaptive treatment strategies. By bridging single-cell resolution with clinical outcomes, our work underscores the transformative potential of multi-omics approaches in precision oncology.

Acknowledgements

This work was funded in part by the Science and Technology Innovation Project of Shaoxing (No. 2024SKY028).

Disclosure of conflict of interest

None.

Address correspondence to: Dr. Jian-Fang Wang, Department of Oncology, Shaoxing People's Hospital, No. 568 Zhongxing North Road, Shaoxing 312000, Zhejiang, China. Tel: +86-0575-88559622; E-mail: sxwxdd@163.com

References

[1] Swetter SM, Johnson D, Albertini MR, Barker CA, Bateni S, Baumgartner J, Bhatia S, Bichakjian C, Boland G, Chandra S, Chmielowski B, DiMaio D, Dronca R, Fields RC, Fleming MD, Galan A, Guild S, Hyngstrom J, Karakousis G, Kendra K, Kiuru M, Lange JR, Lanning R, Logan T, Olson D, Olszanski AJ, Ott PA, Ross MI, Rothermel L, Salama AK, Sharma R, Skitzki J, Smith E, Tsai K, Wuthrick E, Xing Y, McMillian N and Espinosa S. NCCN guidelines® insights: melanoma: cutaneous, version 2.2024. J Natl Compr Canc Netw 2024; 22: 290-298.

[2] Barba I, Carrillo-Bosch L and Seoane J. Targeting the warburg effect in cancer: where do we stand? Int J Mol Sci 2024; 25: 3142.

[3] Kang Y, Yeo M, Choi H, Jun H, Eom S, Park SG, Yoon H, Kim E and Kang S. Lactate oxidase/vSIRPα conjugates efficiently consume tumor-produced lactates and locally produce tumor-necrotic H(2)O(2) to suppress tumor growth. Int J Biol Macromol 2023; 231: 123577.

[4] Cai X, Ng CP, Jones O, Fung TS, Ryu KW, Li D and Thompson CB. Lactate activates the mitochondrial electron transport chain independently of its metabolism. Mol Cell 2023; 83: 3904-3920, e7.

[5] Zhang D, Tang Z, Huang H, Zhou G, Cui C, Weng Y, Liu W, Kim S, Lee S, Perez-Neut M, Ding J, Czyz D, Hu R, Ye Z, He M, Zheng YG, Shuman HA, Dai L, Ren B, Roeder RG, Becker L and Zhao Y. Metabolic regulation of gene expression by histone lactylation. Nature 2019; 574: 575-580.

[6] Yang Z, Yan C, Ma J, Peng P, Ren X, Cai S, Shen X, Wu Y, Zhang S, Wang X, Qiu S, Zhou J, Fan J, Huang H and Gao Q. Lactylome analysis suggests lactylation-dependent mechanisms of metabolic adaptation in hepatocellular carcinoma. Nat Metab 2023; 5: 61-79.

[7] Wan N, Wang N, Yu S, Zhang H, Tang S, Wang D, Lu W, Li H, Delafield DG, Kong Y, Wang X, Shao C, Lv L, Wang G, Tan R, Wang N, Hao H and Ye H. Cyclic immonium ion of lactyllysine reveals widespread lactylation in the human proteome. Nat Methods 2022; 19: 854-864.

[8] Gaffney DO, Jennings EQ, Anderson CC, Marentette JO, Shi T, Schou Oxvig AM, Streeter MD, Johannsen M, Spiegel DA, Chapman E, Roede JR and Galligan JJ. Non-enzymatic lysine lactoylation of glycolytic enzymes. Cell Chem Biol 2020; 27: 206-213, e6.

[9] Tasdogan A, Faubert B, Ramesh V, Ubellacker JM, Shen B, Solmonson A, Murphy MM, Gu Z, Gu W, Martin M, Kasitinon SY, Vandergriff T, Mathews TP, Zhao Z, Schadendorf D, DeBerardinis RJ and Morrison SJ. Metabolic heterogeneity confers differences in melanoma metastatic potential. Nature 2020; 577: 115-120.

[10] Hayes C, Donohoe CL, Davern M and Donlon NE. The oncogenic and clinical implications of lactate induced immunosuppression in the tumour microenvironment. Cancer Lett 2021; 500: 75-86.

[11] Li T, Xu D, Ruan Z, Zhou J, Sun W, Rao B and Xu H. Metabolism/immunity dual-regulation thermogels potentiating immunotherapy of glioblastoma through lactate-excretion inhibition and PD-1/PD-L1 blockade. Adv Sci (Weinh) 2024; 11: e2310163.

[12] Li L, Ji Y, Zhang L, Cai H, Ji Z, Gu L and Yang S. Wogonin inhibits the growth of HT144 melanoma via regulating hedgehog signaling-mediated inflammation and glycolysis. Int Immunopharmacol 2021; 101: 108222.

[13] Yang Z, Zheng Y and Gao Q. Lysine lactylation in the regulation of tumor biology. Trends Endocrinol Metab 2024; 35: 720-731.

[14] Sun T, Liu B, Li Y, Wu J, Cao Y, Yang S, Tan H, Cai L, Zhang S, Qi X, Yu D and Yang W. Oxamate enhances the efficacy of CAR-T therapy against glioblastoma via suppressing ectonucleotidases and CCR8 lactylation. J Exp Clin Cancer Res 2023; 42: 253.

[15] Vettraino M, Manerba M, Govoni M and Di Stefano G. Galloflavin suppresses lactate dehydrogenase activity and causes MYC down-regulation in Burkitt lymphoma cells through NAD/NADH-dependent inhibition of sirtuin-1. Anticancer Drugs 2013; 24: 862-870.

[16] Luengo A, Li Z, Gui DY, Sullivan LB, Zagorulya M, Do BT, Ferreira R, Naamati A, Ali A, Lewis CA, Thomas CJ, Spranger S, Matheson NJ and Vander Heiden MG. Increased demand for NAD(+) relative to ATP drives aerobic glycolysis. Mol Cell 2021; 81: 691-707, e696.

[17] Aibar S, González-Blas CB, Moerman T, Huynh-Thu VA, Imrichova H, Hulselmans G, Rambow F, Marine JC, Geurts P, Aerts J, van den Oord J, Atak ZK, Wouters J and Aerts S. SCENIC: single-cell regulatory network inference and clustering. Nat Methods 2017; 14: 1083-1086.

[18] Jin S, Plikus MV and Nie Q. CellChat for systematic analysis of cell-cell communication from single-cell transcriptomics. Nat Protoc 2025; 20: 180-219.

[19] Huang H, Chen K, Zhu Y, Hu Z, Wang Y, Chen J, Li Y, Li D and Wei P. A multi-dimensional ap-

proach to unravel the intricacies of lactylation related signature for prognostic and therapeutic insight in colorectal cancer. J Transl Med 2024; 22: 211.
[20] Chen B, Khodadoust MS, Liu CL, Newman AM and Alizadeh AA. Profiling tumor infiltrating immune cells with CIBERSORT. Methods Mol Biol 2018; 1711: 243-259.
[21] Johnson WE, Li C and Rabinovic A. Adjusting batch effects in microarray expression data using empirical Bayes methods. Biostatistics 2007; 8: 118-127.
[22] Kleino I, Frolovaitė P, Suomi T and Elo LL. Computational solutions for spatial transcriptomics. Comput Struct Biotechnol J 2022; 20: 4870-4884.
[23] Gajic ZZ, Deshpande A, Legut M, Imieliński M and Sanjana NE. Recurrent somatic mutations as predictors of immunotherapy response. Nat Commun 2022; 13: 3938.
[24] Chen L, Huang L, Gu Y, Cang W, Sun P and Xiang Y. Lactate-lactylation hands between metabolic reprogramming and immunosuppression. Int J Mol Sci 2022; 23: 11943.
[25] Li F, Si W, Xia L, Yin D, Wei T, Tao M, Cui X, Yang J, Hong T and Wei R. Positive feedback regulation between glycolysis and histone lactylation drives oncogenesis in pancreatic ductal adenocarcinoma. Mol Cancer 2024; 23: 90.
[26] Sabbah M, Krayem M, Najem A, Sales F, Miller W, Del Rincon S, Awada A, Ghanem GE and Journe F. Dasatinib stimulates its own mechanism of resistance by activating a CRTC3/MITF/Bcl-2 pathway in melanoma with mutant or amplified c-Kit. Mol Cancer Res 2021; 19: 1221-1233.
[27] Hu S, Huang J, Pei S, Ouyang Y, Ding Y, Jiang L, Lu J, Kang L, Huang L, Xiang H, Xiao R, Zeng Q and Chen J. Ganoderma lucidum polysaccharide inhibits UVB-induced melanogenesis by antagonizing cAMP/PKA and ROS/MAPK signaling pathways. J Cell Physiol 2019; 234: 7330-7340.
[28] Tangudu NK, Buj R, Wang H, Wang J, Cole AR, Uboveja A, Fang R, Amalric A, Yang B, Chatoff A, Crispim CV, Sajjakulnukit P, Lyons MA, Cooper K, Hempel N, Lyssiotis CA, Chandran UR, Snyder NW and Aird KM. De Novo purine metabolism is a metabolic vulnerability of cancers with low p16 expression. Cancer Res Commun 2024; 4: 1174-1188.
[29] Lu N, Guan X, Bao W, Fan Z and Zhang J. Breast cancer combined prognostic model based on lactate metabolism genes. Medicine (Baltimore) 2022; 101: e32485.
[30] Huang A, Sun Z, Hong H, Yang Y, Chen J, Gao Z and Gu J. Novel hypoxia- and lactate metabolism-related molecular subtyping and prognostic signature for colorectal cancer. J Transl Med 2024; 22: 587.
[31] Gao Y, Liu H, Wan J, Chang F, Zhang L, Wang W, Zhang Q and Feng Q. Construction and assessment of a prognostic risk model for cervical cancer based on lactate metabolism-related lncRNAs. Int J Gen Med 2023; 16: 2943-2960.
[32] Xie J, Zhang P, Ma C, Tang Q, Zhou X, Xu X, Zhang M, Zhao S, Zhou L and Qi M. Unravelling the metabolic landscape of cutaneous melanoma: Insights from single-cell sequencing analysis and machine learning for prognostic assessment of lactate metabolism. Exp Dermatol 2024; 33: e15119.
[33] Zhu Y, Song B, Yang Z, Peng Y, Cui Z, Chen L and Song B. Integrative lactylation and tumor microenvironment signature as prognostic and therapeutic biomarkers in skin cutaneous melanoma. J Cancer Res Clin Oncol 2023; 149: 17897-17919.
[34] Geissler R, Golbik RP and Behrens SE. The DEAD-box helicase DDX3 supports the assembly of functional 80S ribosomes. Nucleic Acids Res 2012; 40: 4998-5011.
[35] Pan Y, Zhu Y, Zhang J, Jin L and Cao P. A feedback loop between GATA2-AS1 and GATA2 promotes colorectal cancer cell proliferation, invasion, epithelial-mesenchymal transition and stemness via recruiting DDX3X. J Transl Med 2022; 20: 287.
[36] Atkinson SC, Heaton SM, Audsley MD, Kleifeld O and Borg NA. TRIM25 and DEAD-Box RNA helicase DDX3X cooperate to regulate RIG-I-mediated antiviral immunity. Int J Mol Sci 2021; 22: 9094.
[37] Zhang MX, Gan W, Jing CY, Zheng SS, Yi Y, Zhang J, Xu X, Lin JJ, Zhang BH and Qiu SJ. S100A11 promotes cell proliferation via P38/MAPK signaling pathway in intrahepatic cholangiocarcinoma. Mol Carcinog 2019; 58: 19-30.
[38] Cimica V, Chen HC, Iyer JK and Reich NC. Dynamics of the STAT3 transcription factor: nuclear import dependent on Ran and importin-β1. PLoS One 2011; 6: e20188.
[39] Kemp C, Coleman A, Wells G and Parry G. Overexpressing components of the nuclear transport apparatus causes severe growth symptoms in tobacco leaves. Plant Signal Behav 2015; 10: e1000103.
[40] Tong J, Xu X, Zhang Z, Ma C, Xiang R, Liu J, Xu W, Wu C, Li J, Zhan F, Wu Y and Yan H. Hypoxia-induced long non-coding RNA DARS-AS1 regulates RBM39 stability to promote myeloma malignancy. Haematologica 2020; 105: 1630-1640.
[41] Vohhodina J, Barros EM, Savage AL, Liberante FG, Manti L, Bankhead P, Cosgrove N, Madden AF, Harkin DP and Savage KI. The RNA processing factors THRAP3 and BCLAF1 promote the DNA damage response through selective

mRNA splicing and nuclear export. Nucleic Acids Res 2017; 45: 12816-12833.
[42] Li L, Li F, Hu X, Wu Z, Ren W, Wang T, Ji Z, Li N, Gu J, Sun C, Feng X, Han W, Huang J and Lei L. LAP3 contributes to IFN-γ-induced arginine depletion and malignant transformation of bovine mammary epithelial cells. BMC Cancer 2022; 22: 864.
[43] El-Tanani M, Nsairat H, Mishra V, Mishra Y, Aljabali AAA, Serrano-Aroca Á and Tambuwala MM. Ran GTPase and its importance in cellular signaling and malignant phenotype. Int J Mol Sci 2023; 24: 3065.
[44] Liu Y, Song J, Shi Q, Chen B, Qiu W, Liu Y, Huang S and He X. Glucose-induced LINC01419 reprograms the glycolytic pathway by recruiting YBX1 to enhance PDK1 mRNA stability in hepatocellular carcinoma. Clin Transl Med 2024; 14: e70122.
[45] Zhang X, Wei Z, Yong T, Li S, Bie N, Li J, Li X, Liu H, Xu H, Yan Y, Zhang B, Chen X, Yang X and Gan L. Cell microparticles loaded with tumor antigen and resiquimod reprogram tumor-associated macrophages and promote stem-like CD8(+) T cells to boost anti-PD-1 therapy. Nat Commun 2023; 14: 5653.
[46] Cervantes-Villagrana RD, Albores-García D, Cervantes-Villagrana AR and García-Acevez SJ. Tumor-induced neurogenesis and immune evasion as targets of innovative anti-cancer therapies. Signal Transduct Target Ther 2020; 5: 99.
[47] Tang C, Welsh JW, de Groot P, Massarelli E, Chang JY, Hess KR, Basu S, Curran MA, Cabanillas ME, Subbiah V, Fu S, Tsimberidou AM, Karp D, Gomez DR, Diab A, Komaki R, Heymach JV, Sharma P, Naing A and Hong DS. Ipilimumab with stereotactic ablative radiation therapy: phase I results and immunologic correlates from peripheral T cells. Clin Cancer Res 2017; 23: 1388-1396.
[48] Steinberg SM, Shabaneh TB, Zhang P, Martyanov V, Li Z, Malik BT, Wood TA, Boni A, Molodtsov A, Angeles CV, Curiel TJ, Whitfield ML and Turk MJ. Myeloid cells that impair immunotherapy are restored in melanomas with acquired resistance to BRAF inhibitors. Cancer Res 2017; 77: 1599-1610.
[49] Seth P, Csizmadia E, Hedblom A, Vuerich M, Xie H, Li M, Longhi MS and Wegiel B. Deletion of lactate dehydrogenase-A in myeloid cells triggers antitumor immunity. Cancer Res 2017; 77: 3632-3643.
[50] Xiao X, Mo H and Tu K. CTNNB1 mutation suppresses infiltration of immune cells in hepatocellular carcinoma through miRNA-mediated regulation of chemokine expression. Int Immunopharmacol 2020; 89: 107043.
[51] Lv Q, Zhang Y, Gao W, Wang J, Hu Y, Yang H, Xie Y, Lv Y, Zhang H, Wu D, Hu L and Wang J. CSF1R inhibition reprograms tumor-associated macrophages to potentiate anti-PD-1 therapy efficacy against colorectal cancer. Pharmacol Res 2024; 202: 107126.
[52] Gaur V, Tyagi W, Das S, Ganguly S and Bhattacharyya J. CD40 agonist engineered immunosomes modulated tumor microenvironment and showed pro-immunogenic response, reduced toxicity, and tumor free survival in mice bearing glioblastoma. Biomaterials 2024; 311: 122688.
[53] Wuerdemann N, Pütz K, Eckel H, Jain R, Wittekindt C, Huebbers CU, Sharma SJ, Langer C, Gattenlöhner S, Büttner R, Speel EJ, Suchan M, Wagner S, Quaas A and Klussmann JP. LAG-3, TIM-3 and VISTA expression on tumor-infiltrating lymphocytes in oropharyngeal squamous cell carcinoma-potential biomarkers for targeted therapy concepts. Int J Mol Sci 2020; 22: 379.
[54] Kong YZ, Chen Q and Lan HY. Macrophage migration inhibitory factor (MIF) as a stress molecule in renal inflammation. Int J Mol Sci 2022; 23: 4908.
[55] Ge J, Chen J, Shen Q, Zheng X, Chen X, Shi L, Chen L and Xu B. Comprehensive analysis of the immunosuppressive function of regulatory T cells in human hepatocellular carcinoma tissues. Cancer Control 2024; 31: 10732748241251580.
[56] Richard V, Kindt N and Saussez S. Macrophage migration inhibitory factor involvement in breast cancer (review). Int J Oncol 2015; 47: 1627-1633.
[57] Huang ZW, Zhang XN, Zhang L, Liu LL, Zhang JW, Sun YX, Xu JQ, Liu Q and Long ZJ. STAT5 promotes PD-L1 expression by facilitating histone lactylation to drive immunosuppression in acute myeloid leukemia. Signal Transduct Target Ther 2023; 8: 391.
[58] Chen J, Huang Z, Chen Y, Tian H, Chai P, Shen Y, Yao Y, Xu S, Ge S and Jia R. Lactate and lactylation in cancer. Signal Transduct Target Ther 2025; 10: 38.
[59] Friis RMN, Glaves JP, Huan T, Li L, Sykes BD and Schultz MC. Rewiring AMPK and mitochondrial retrograde signaling for metabolic control of aging and histone acetylation in respiratory-defective cells. Cell Rep 2014; 7: 565-574.
[60] Li X, Peng X, Li Y, Wei S, He G, Liu J, Li X, Yang S, Li D, Lin W, Fang J, Yang L and Li H. Glutamine addiction in tumor cell: oncogene regulation and clinical treatment. Cell Commun Signal 2024; 22: 12.

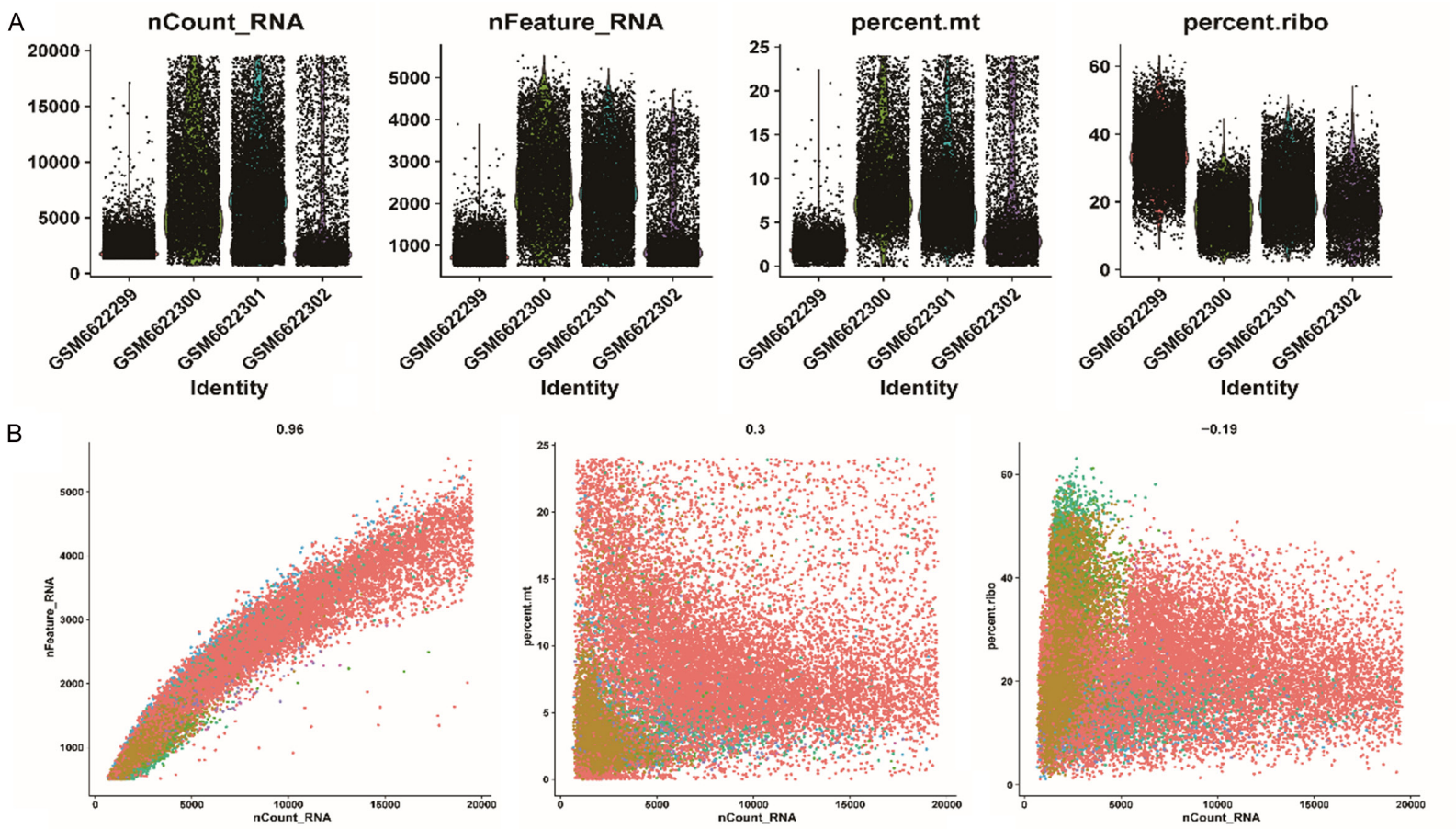
A
nCount_RNA
nFeature_RNA
percent.mt
percent.ribo
GSM6622299
GSM6622300
GSM6622301
GSM6622302
Identity
B
0.96
0.3
−0.19
nFeature_RNA
percent.mt
percent.ribo
nCount_RNA

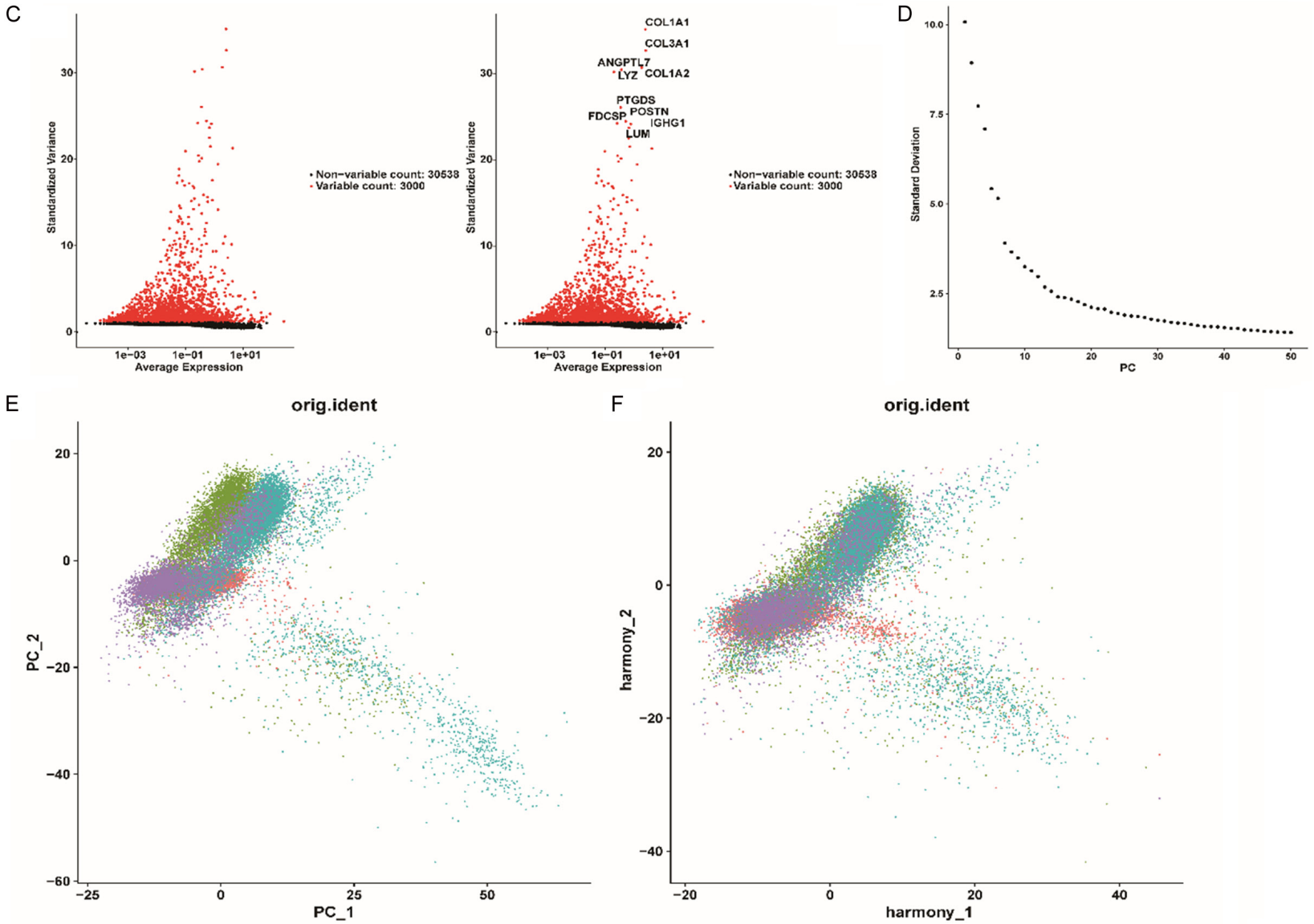

Figure S1. Preprocessing of single-cell expression data. A. Violin plots showing gene counts, unique molecular identifiers (UMIs), and mitochondrial read proportions per cell in GSM6622299, GSM6622300, GSM6622301, and GSM6622302. B. Scatter plots of filtered versus unfiltered cells, reflecting quality control outcomes. C. Top 10 genes with highest standard deviation. D. Elbow plot revealing the first 20 principal components (PCs) selected for dimensionality reduction. E. PCA-based assessment of batch effects among samples. F. Batch effect correction via Harmony.

Figure S2. Metabolic and immune pathway activities of model genes. Bubble plots visualizing AUCell-based quantification of immune/metabolic pathway engagement in single cells. THRAP3 and S100A11 were strongly linked to oxidative phosphorylation and MYC targets, while RBM39, RAN, LAP3, and DDX3X exhibited associations with immune evasion and oncogenic signaling.

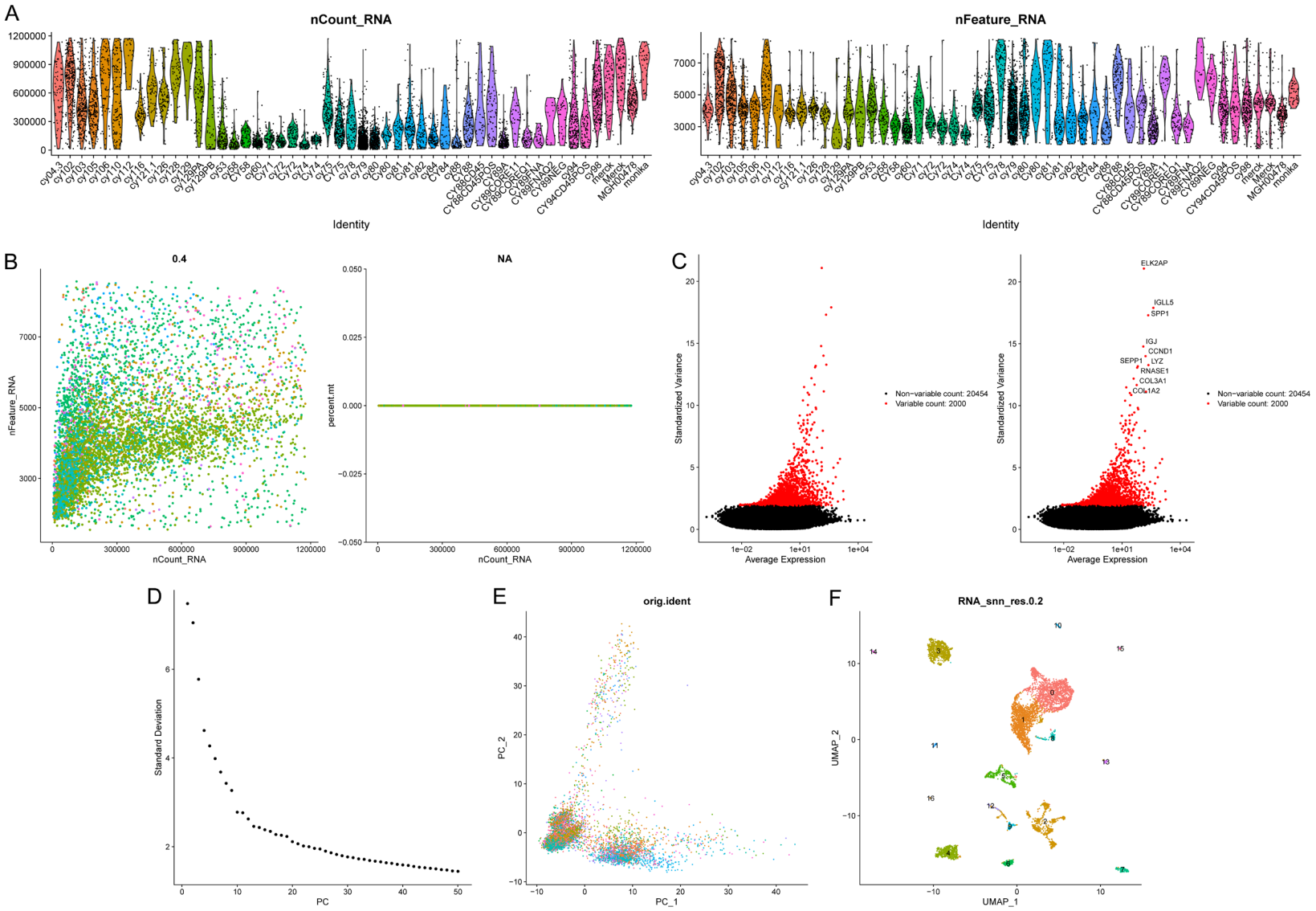

Figure S3. Quality control and clustering of scRNA-seq data from GSE115978. A. Violin plots showing distributions of detected genes, UMIs, and mitochondrial gene percentages across 20 melanoma samples before (left) and after (right) quality control filtering. Dashed lines indicate filtering thresholds. B. Scatter plots visualizing post-filtering metrics (n = 6,404 cells): gene counts vs. UMIs (left), and gene counts vs. mitochondrial percentages (right). C. Dot plot of the top 10 highly variable genes across cells after normalization. D. Elbow plot determining the optimal number of principal components (PCs = 20) for dimensionality reduction. E. PCA plot before batch correction, revealing significant inter-sample batch effects. F. UMAP visualization of 6,404 cells clustered into 17 transcriptionally distinct subpopulations after Harmony batch correction.

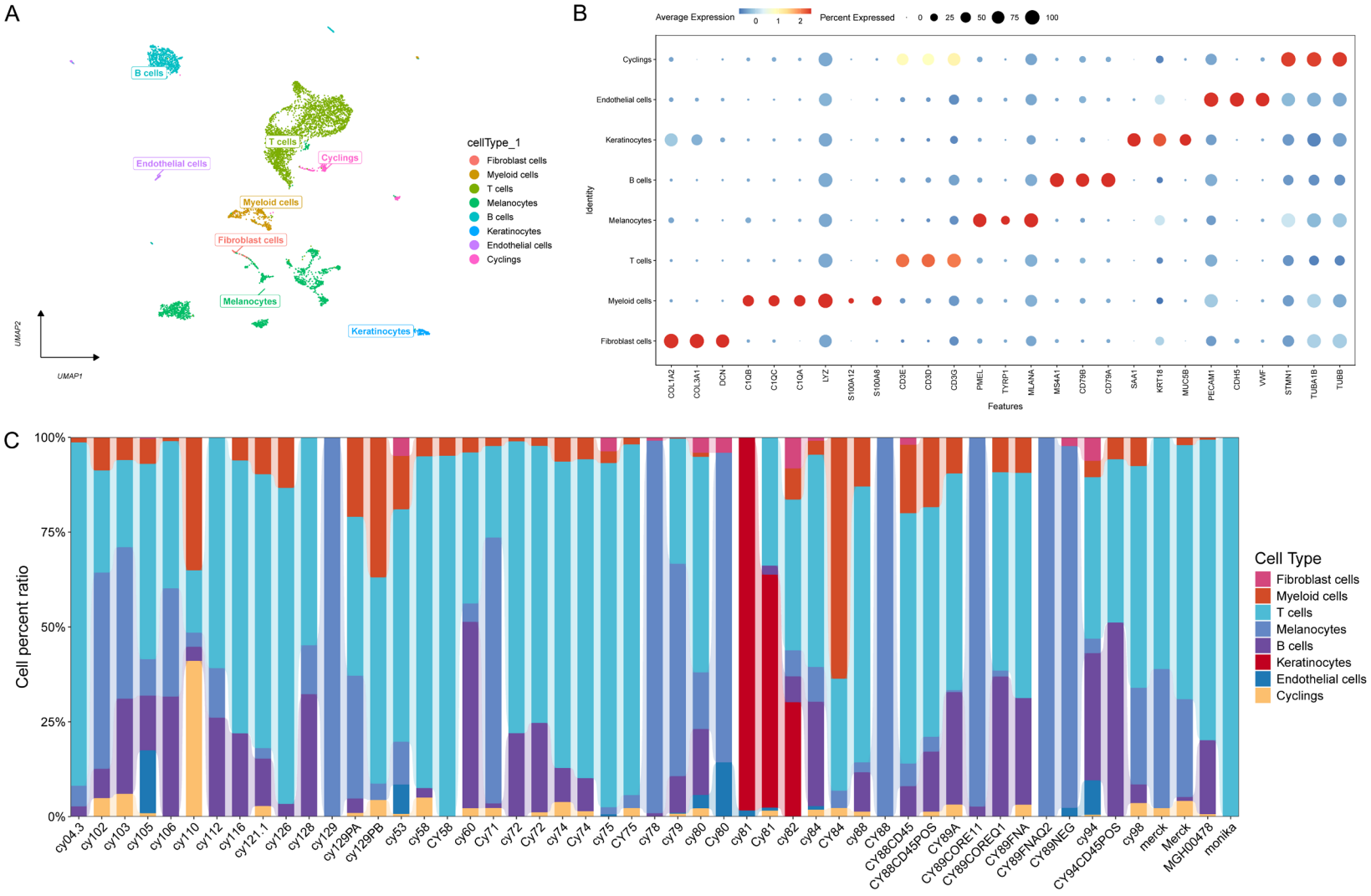

Figure S4. Cell type annotation for the GSE115978 scRNA-seq dataset. A. UMAP plot annotating 17 clusters into 8 major cell types using canonical markers. B. Bubble plot displaying expression intensity (color) and percentage (size) of marker genes across cell types. C. Stacked bar chart illustrating the proportional distribution of cell types across all samples.

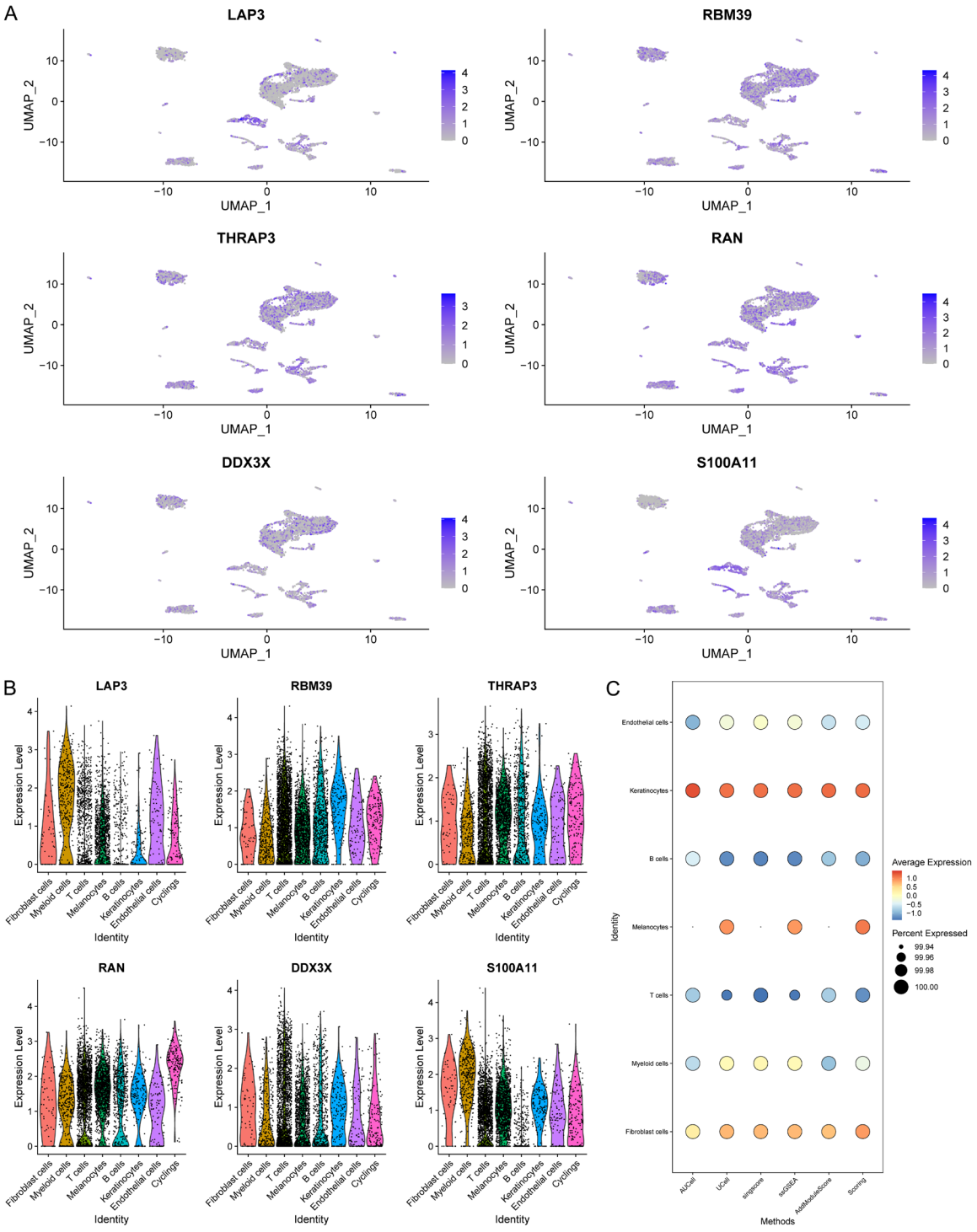
A
LAP3
RBM39
THRAP3
RAN
DDX3X
S100A11
UMAP_1
UMAP_2
B
Expression Level
Identity
Fibroblast cells
Myeloid cells
T cells
Melanocytes
B cells
Keratinocytes
Endothelial cells
Cyclings
C
Identity
Methods
AUCell
UCell
singscore
ssGSEA
AddModuleScore
Scoring
Average Expression
Percent Expressed
99.94
99.96
99.98
100.00

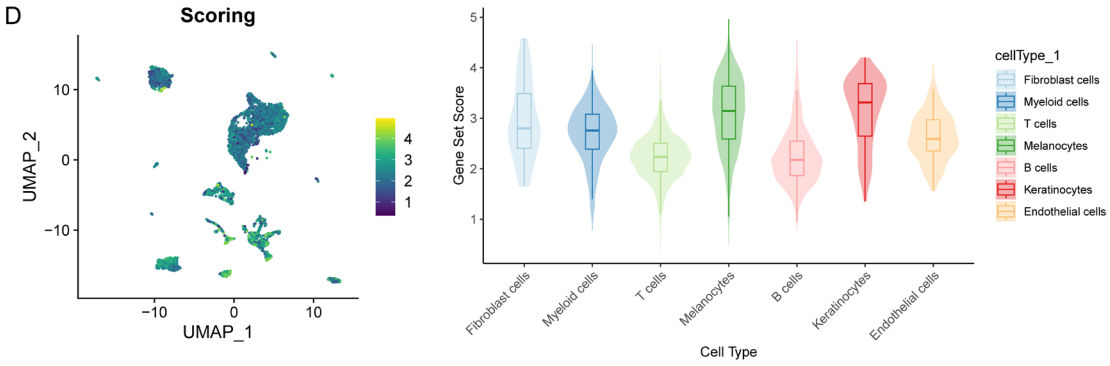

Figure S5. Key Gene Expression and Lactylation Scoring in Melanoma scRNA-seq Data (GSE115978). A, B. DotPlot and Violin plots visualizing expression of prognostic signature genes (LAP3, RBM39, THRAP3, RAN, DDX3X, S100A11). C. Bubble plot showing multi-algorithm quantification of lactylation scores (AUCell, UCell, singscore, ssGSEA, AddModuleScore) averaged across cell types. D. DotPlot and Violin plots confirm significantly elevated lactylation activity in melanocytes ($P < 0.001$).